

The Role of Peroxins 1 and 6 in the Retinal Pigment Epithelium

by

Constantin Mouzaaber

A thesis submitted in partial fulfillment of the requirements for the degree of

Master of Science

Medical Sciences - Ophthalmology and Visual Sciences

University of Alberta

© Constantin Mouzaaber, 2024

ABSTRACT

Purpose. Peroxisomes are ubiquitous organelles that compartmentalize metabolic reactions including lipid catabolism and cellular detoxification. Enzymes flagged by peroxisomal targeting sequences are delivered into peroxisomes by the cumulative action of some peroxins (PEX), including PEX5 which shuttles the enzymes. Peroxisome biogenesis disorders (PBDs) are recessive conditions caused by biallelic loss-of-function mutations in genes responsible for peroxisome assembly and function. Approximately two-thirds of PBDs are caused by mutations in *PEX1* or *PEX6*, which encode PEX1 and 6, respectively. Together, PEX1 and PEX6 form an ATPase Associated with diverse cellular Activities (AAA ATPase) exportomer that facilitates the release of monoubiquitinated PEX5 from the peroxisomal membrane to accommodate further shuttling of peroxisome enzymes. The RPE is a specialized monolayer of cells that performs several critical roles in the retina, including the daily phagocytosis of light-sensitive photoreceptor outer segments (POS), facilitating their renewal. PBDs are frequently associated with retinal pigment epithelial (RPE) dysfunction and retinal degeneration, but precisely how impaired peroxisome activity perturbs retinal function remains to be fully explored. Effective degradation of the lipid-rich POS ingested by the RPE is hypothesized to depend on intact and functional peroxisomes. This project aims to study the effects of peroxisome dysfunction in the RPE and highlight the importance of intact peroxisomes in maintaining normal vision.

Methods. To study the effects of a severe PBD genotype, *PEX1* and *PEX6* knockout (KO) induced pluripotent stem cells (iPSCs), along with the isogenic wild-type iPSCs, were differentiated into RPE cells (iRPE) in culture. Immunoblot analysis of whole iRPE cell lysates was performed, and the processing of ACAA1, a peroxisome matrix protein, was evaluated to assess the fidelity of peroxisome matrix protein import in the *PEX1* KO and *PEX6* KO iRPE cells relative to wild-type. Immunofluorescence detection of an antibody against PMP70, a peroxisomal membrane protein, in combination with image analysis were used to determine the abundance of peroxisomes across iRPE cell lines. Gas chromatography with flame-ionization detection was used to quantitatively compare the fatty acid lipid profiles of the wild-type and *PEX6* KO iRPE. POS isolated from bovine eyes were added to iRPE cell culture media to examine the effect of *PEX1* and *PEX6* mutation on POS phagocytosis in iRPE. Immunofluorescence experiments focused upon lipid droplets were performed to interrogate lipid accumulation in iRPE. Flow cytometry experiments were performed to assess the heterogeneity of the differentiated iRPE populations and quantify the intracellular neutral lipid content of the cells before and after addition of isolated POS.

Results. Fewer PMP70-positive puncta were observed in *PEX1* KO and *PEX6* KO iRPE, but no statistical significance was reached ($P= 0.29$). Immunoblot analysis demonstrated disrupted processing of matrix-destined ACAA1, likely due to impaired peroxisome exportome machinery in *PEX1* KO and *PEX6* KO iRPE cells. *PEX6* KO iRPE had significantly reduced levels of docosahexaenoic acid (DHA) ($P<0.0001$), a long-chain

polyunsaturated fatty acid that can be generated by peroxisomes but is largely acquired from diet. Additionally, *PEX6* KO iRPE significantly accumulated DHA-precursor fatty acids ($P < 0.0001$). At baseline, *PEX1* KO and *PEX6* KO iRPE cells exhibited an increased number of lipid droplets, and contained significantly more intracellular neutral lipids relative to wild-type iRPE ($P = 0.0005$ and $P < 0.0001$, respectively). After challenging the cells with POS, *PEX1* KO and *PEX6* KO iRPE exhibited an increased size and number of lipid droplets, and demonstrated significantly elevated binding of dyes for intracellular neutral lipids relative to wild-type iRPE ($P < 0.0001$).

Conclusions. This work established the first human iRPE culture model to study the effects of peroxisome dysfunction. *PEX1* KO and *PEX6* KO iRPE displayed impaired peroxisomal matrix protein import. Peroxisome dysfunction induced significant lipid profile changes in iRPE cells, including elevated very long-chain fatty acids and reduced DHA. *PEX1* KO and *PEX6* KO iRPE accumulated intracellular lipid droplets, which is a biomarker of aged and diseased RPE. Challenging iRPE with POS aggravated an already significant lipid handling defect in the *PEX1* KO and *PEX6* KO iRPE. A better understanding of the role of peroxisomes in the RPE will facilitate the development of novel therapeutic approaches for patients with peroxisomal disorders and retinal degeneration.

PREFACE

This thesis is an original work by Constantin Mouzaaber. The research project, of which this thesis is a part, received research ethics approval from the University of Alberta Research Ethics Board, “Characterizing the Effect of PEX6 Mutations on Peroxisome Function in the Retinal Pigment Epithelium”, No. Pro00074451.

ACKNOWLEDGEMENTS

I would like to sincerely thank everyone in the Department of Ophthalmology and Visual Sciences for cultivating a positive learning environment. I learned from all of my interactions with faculty and staff members. I am continuously inspired by department role models as I received generous support throughout my program. I would also like to acknowledge the Department of Cell Biology and the Department of Physiology for always warmly welcoming my inquiries. I am extremely grateful for the connections that I fostered with the excellent community of researchers and trainees at the University of Alberta.

I would like to thank Dr. Jennifer Hocking for enabling my participation in undergraduate vision research. Her lab strongly equipped me to pursue my graduate education. I would like to thank my lab mates for supporting my work and pushing me to pursue research excellence.

Additionally, I would like to warmly thank my supervisory committee members, Dr. Brittany Carr, Dr. Ian MacDonald, and Dr. Andrew Simmonds for guiding me throughout my degree.

Most importantly, I would like to thank my supervisor Dr. Matthew Benson for trusting me with this project. Dr. Benson effectively established the basis of my research. I was able to effortlessly share my scientific passion with Dr. Benson. I am lucky to have had the most caring, understanding, and supportive supervisor.

I would like to thank the University of Alberta Research Cores: Lipidomics, Imaging, Flow Cytometry, and Advanced Cell Exploration for facilitating my research.

I want to acknowledge the Canadian Institutes of Health Research, Funding Blindness Canada, Bayer, Sigma Xi, the Government of Alberta, the Department of Ophthalmology and Visual Sciences, and the University of Alberta for funding my studies.

If you were a part of this journey, thank you.

Table of Contents

| | |
|--|-----|
| Title Page..... | i |
| ABSTRACT | ii |
| PREFACE | v |
| ACKNOWLEDGEMENTS..... | vi |
| List of tables | ix |
| List of Figures | x |
| List of Abbreviations | xii |
| 1. Introduction..... | 1 |
| 1.1 Peroxisomes | 1 |
| 1.2 The Role of PEX1 and PEX6 in Matrix Protein Import and Pexophagy | 2 |
| 1.3 Peroxisome Biogenesis Disorders | 4 |
| 1.4 Photoreceptors | 5 |
| 1.5 Retinal Pigment Epithelium..... | 7 |
| 1.6 Lipid Droplets | 8 |
| 1.7 Lipid Metabolism in the Retinal Pigment Epithelium..... | 9 |
| 1.8 Role of Peroxisomes in the Retinal Pigment Epithelium | 9 |
| 1.9 Hypothesis | 10 |
| 2. Methods | 11 |
| 2.1 Cell Culture | 11 |
| 2.2 Generating iRPE (Induced Pluripotent Stem Cells to Retinal Pigment Epithelium) | 12 |
| 2.3 DNA Sanger Sequencing | 14 |
| 2.3.1 PEX1 Knockout Validation | 14 |
| 2.3.2 PEX6 Knockout Validation | 15 |
| 2.4 Western Blotting | 15 |
| 2.5 Immunofluorescence | 17 |
| 2.6 Flow Cytometry | 18 |
| 2.7 Mass Spectrometry | 20 |

| | |
|--|----|
| 2.8 Photoreceptor Outer Segments Isolation..... | 21 |
| 2.10 Statistics | 24 |
| 3. Results | 25 |
| 3.1 Differentiation of Induced Pluripotent Stem Cells to Retinal Pigment Epithelium. | 25 |
| 3.2 Validation of Retinal Pigment Epithelium (iRPE) | 26 |
| 3.3 Evaluation of Peroxisomes in the Retinal Pigment Epithelium..... | 28 |
| 3.3.1 Verification of PEX1 and PEX6 Knockouts | 28 |
| 3.3.2 Peroxisome Abundance | 29 |
| 3.3.3 Peroxisomal Matrix Protein Import | 31 |
| 3.4 Lipid Profiles of the Retinal Pigment Epithelium (iRPE)..... | 33 |
| 3.5 Photoreceptor Outer Segment Challenge..... | 35 |
| 3.5.1 Immunofluorescence..... | 35 |
| 3.5.2 Flow Cytometry | 37 |
| 4. Discussion..... | 39 |
| 4.1 Effectiveness of a Human Stem-Cell Derived Model of Peroxisome Dysfunction in the Retinal Pigment Epithelium | 39 |
| 4.2 <i>Differentiation of PEX1 and PEX6 Knockout Retinal Pigment Epithelium</i> | 43 |
| 4.3 Lipid Profiles in Retinal Pigment Epithelium with Abnormal Peroxisome Function | 44 |
| 4.4 Study Limitations | 48 |
| 4.5 Future Directions | 49 |
| 4.5.1 Generating Patient-Derived Retinal Pigment Epithelium | 49 |
| 4.5.2 DHA Supplementation | 50 |
| 4.5.3 Mimicking Photoreceptor Outer Segment Lipids Using Synthetic Liposomes | 50 |
| 4.6 Concluding Remarks | 51 |
| References | 52 |
| Appendix | 70 |

List of tables

| | |
|---|----|
| Table 1. List of antibodies with corresponding application and concentration..... | 23 |
| Table 2. Detecting RPE signature proteins using flow cytometry to validate PEX1 KO, PEX6 KO, and wild-type iRPE | 27 |

List of Figures

| | |
|--|----|
| Figure 1. A model of peroxisomal matrix protein import and receptor export..... | 3 |
| Figure 2. Consequences of PEX1 or PEX6 dysfunction on peroxisome abundance and activity | 5 |
| Figure 3. Anatomical relationship between a retinal pigment epithelial (RPE) cell and the apical side of a photoreceptor cell..... | 6 |
| Figure 4. Differentiation stages and timeline for the conversion of iPSC to RPE. | 26 |
| Figure 5. Pigmentation and basal fluid pumping in iRPE..... | 28 |
| Figure 6. Confirmation of PEX1 and PEX6 knockout at the DNA and protein levels | 29 |
| Figure 7. Quantification of PMP70-positive puncta as a measure of peroxisome abundance in iRPE..... | 30 |
| Figure 8. Evaluating peroxisome matrix protein import by assessing ACAA1 distribution and processing. | 32 |
| Figure 9. A comparison of the fatty acid profiles of PEX6 KO and wild-type iRPE | 35 |
| Figure 10. Immunofluorescence detection of lipid accumulation in iRPE following photoreceptor outer segment challenge | 36 |
| Figure 11. Flow cytometry-based quantification of lipid accumulation in iRPE following POS challenge..... | 37 |
| Supplementary Figure 1. Visualizing photoreceptor outer segments isolated from bovine retinas..... | 70 |
| Supplementary Figure 2. Immunofluorescence detection of ZO-1 in iRPE | 70 |
| Supplementary Figure 3. Immunofluorescence detection of PMP70 in iRPE..... | 71 |
| Supplementary Figure 4. Quantification of PMP70-positive puncta in iRPE..... | 71 |
| Supplementary Figure 5. Evaluating ACAA1 processing by western blot to assess the integrity of peroxisomal matrix protein import. | 72 |

Supplementary Figure 6. Immunofluorescence detection of PLIN2 and Claudin-19 in wild-type iRPE fed with POS. 72

Supplementary Figure 7. Western blot standard curves for PMP70 and ACAA1. 73

List of Abbreviations

| | |
|---------------|--|
| AAA | ATPases Associated with Diverse Cellular Activities |
| ACAA1 | Acetyl-Coenzyme A Acyltransferase 1 |
| ABCD3 | ATP Binding Cassette Subfamily D Member 3 |
| ACOX1 | Acyl-Coenzyme A Oxidase 1 |
| ATGL | Adipose Triglyceride Lipase |
| DHA | Docosahexaenoic Acid |
| DMEM | Dulbecco's Modified Eagle Medium |
| DPBS | Dulbecco's Phosphate Buffered Saline |
| dNTPs | Deoxynucleotide Triphosphates |
| ER | Endoplasmic Reticulum |
| FAs | Fatty Acids |
| FBS | Fetal Bovine Serum |
| FSC | Forward Scatter |
| GS-FID | Gas Chromatography – Flame Ionization Detection |
| iPSC | Induced Pluripotent Stem Cells |
| iRPE | iPSC-Derived Retinal Pigment Epithelium |
| KO | Knockout |
| LDs | Lipid Droplets |
| MFI | Mean Fluorescence Intensity |

| | |
|---------------|---|
| PBDs | Peroxisome Biogenesis Disorders |
| PBS | Phosphate Buffered Saline |
| PBS-T | Phosphate Buffered Saline with Tween-20 |
| PCR | Polymerase Chain Reaction |
| PMP | Peroxisomal Membrane Protein |
| POS | Photoreceptor Outer Segments |
| PTS1 | Peroxisomal Targeting Signal-1 |
| PTS2 | Peroxisomal Targeting Signal-2 |
| RPE | Retinal Pigment Epithelium |
| SSC | Side Scatter |
| TAE | Tris-acetate-ethylenediaminetetraacetic acid |
| TG | Triglycerides |
| VLCFAs | Very Long-Chain Fatty Aci |

1. Introduction

1.1 Peroxisomes

Peroxisomes are dynamic subcellular organelles that have critical roles in lipid metabolism and cellular detoxification. Peroxisomes generate hydrogen peroxide as a byproduct of β -oxidation, hence the organelle nomenclature. Peroxisomes proliferate by growth and division from existing peroxisomes or by *de novo* synthesis from the endoplasmic reticulum (ER). A group of genes referred to as PEX genes encode proteins of various functions called peroxins that support the biogenesis of peroxisomes (Distel et al., 1996). Enzymes destined for peroxisomal matrix localization often contain a peroxisomal targeting sequence (PTS), a C-terminus PTS1 or an N-terminus PTS2 (Figure 1). PEX5 and PEX7 are peroxins that recognize PTS1 and PTS2, respectively (Subramani, 1998). β -ketothiolase or acetyl-coenzyme A acyltransferase 1 (ACAA1) is an enzyme that contains a PTS2 signal, which is a 9 amino acid sequence (Petriv et al., 2004). Once the protein is shuttled inside the peroxisomal lumen, trypsin-like peroxisomal matrix peptidase 1 (TYSND1) cleaves the PTS2 nonapeptide off ACAA1 (Kurochkin et al., 2007; Mizuno et al., 2013). Various peroxisomal membrane proteins (not categorized as peroxins) also support the compartmentalization of reactions inside peroxisomes. For example, ATP-binding cassette, subfamily D, member 3 (ABCD3) also called peroxisomal membrane protein, 70 kDa (PMP70) is an active transporter of long-chain unsaturated fatty acids into the peroxisomal lumen (Ranea-Robles et al., 2021; Van Roermund et al., 2014). Very long-chain fatty acids (VLCFAs) must first be oxidized by peroxisomes because their import into the mitochondria is limited. Peroxisomes preferably oxidize VLCFAs but may also participate in the breakdown of shorter-chain fatty acids of 12 to 16 carbon molecules (Violante et al., 2019). Certain products are specifically generated by peroxisomes such as docosahexaenoic acid (DHA), a 22-carbon long-chain fatty acid with 6 double bonds, the first of which is located at the third carbon from the methyl end (C22:6n3) (Swinkels & Baes, 2023). Canonical peroxisome degradation is initiated by the

recognition of monoubiquitinated PEX5, which accumulates at the organelle surface, by autophagy receptors (Wanders et al., 2023).

1.2 The Role of PEX1 and PEX6 in Matrix Protein Import and Pexophagy

Despite having distinct functions, some peroxins interact with each other to facilitate peroxisomal biogenesis. Peroxisomal enzymes are trafficked inside the organelle after interacting with the cytosolic receptors PEX5 or PEX7. PEX5 has two isoforms, a shorter isoform that shuttles PTS1 tagged proteins, and a longer essential isoform that co-shuttles PTS2 tagged proteins with PEX7. The cargo-containing PEX5 complex docks at PEX13 and PEX14, located at the peroxisome membrane, to translocate proteins into the lumen (Barros-Barbosa et al., 2019). PEX13 forms a pore to facilitate the import of folded and oligomeric proteins into the peroxisomal lumen (Gao et al., 2022). Together, PEX2, PEX10, and PEX12 form an E3 ubiquitin ligase that acts on PEX5 and facilitates its export (Feng, Skowyra, et al., 2022; Feng, Wu, et al., 2022). Polyubiquitination of PEX5 induces its degradation. Monoubiquitination of PEX5 promotes its recycling back to the cytosol through the actions of an ATPase Associated with Diverse Cellular Activities (AAA) that is jointly formed by alternating subunits of PEX1 and PEX6 assembled as a heterohexamer. PEX26 spans the peroxisomal membrane and binds PEX6, facilitating the attachment of the complex to the organelle (Judy et al., 2022). Following the shuttling of peroxisome-destined cargo, the function of the PEX1 and PEX6 AAA ATPase exportomer complex is essential for the release of monoubiquitinated PEX5 back to the cytosol (Figure 1). When the AAA ATPase complex is malfunctioning, monoubiquitinated PEX5 accumulates at the peroxisomal membrane and induces pexophagy, the degradation of peroxisomes by autophagosomes (Law et al., 2017; Wang & Subramani, 2017). Additionally, the reduced amount of cytosolic PEX5 hinders peroxisomal matrix protein import (Figure 2). Disease-causing mutations in *PEX1* and *PEX6* disrupt the function of the exportomer complex and together account for approximately two-thirds of peroxisome biogenesis disorders (PBDs) (Tan et al., 2018).

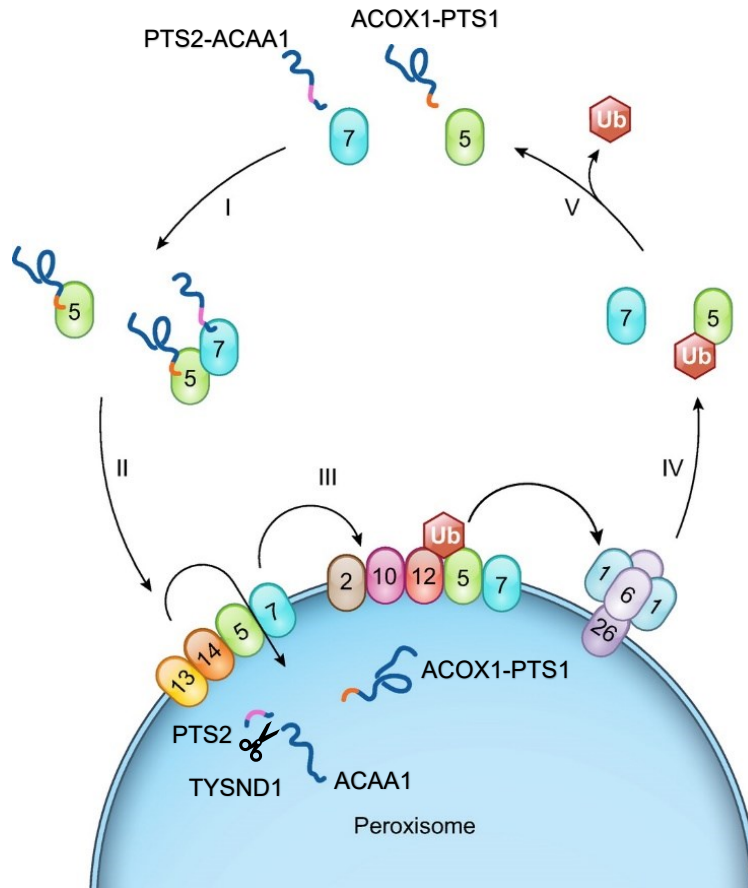


Figure 1. A model of peroxisomal matrix protein import and receptor export. The numbered oval shapes represent peroxin proteins. PEX5 recognizes PTS1-flanked proteins such as acyl-coenzyme A oxidase 1 (ACOX1). PEX7 recognizes PTS2-flanked proteins such as acetyl-coenzyme A acyltransferase 1 (ACAA1). PEX13 and PEX14 support docking and import of the cargo-bound PEX5 and PEX7 shuttles. Once inside the peroxisomal lumen, trypsin-like peroxisomal matrix peptidase 1 (TYSD1) cleaves PTS2 off ACAA1. The PEX2, PEX10, PEX12 E3 ligase complex monoubiquitinates PEX5. The PEX1 and PEX6 AAA ATPase complex facilitates the release of membrane-bound monoubiquitinated PEX5, facilitating subsequent rounds of import. Adapted from Wanders et al., 2023.

1.3 Peroxisome Biogenesis Disorders

Peroxisome biogenesis disorders (PBDs) are severe multisystem diseases that result from defective peroxisome generation and function, and are attributed to biallelic pathogenic mutations in PEX genes. Clinical manifestations are dependent on the remaining operational capacity of the peroxisomal machinery. A spectrum of clinical presentations includes sensory defects, development delays, and neurodegenerative diseases (Fujiki et al., 2020). The more integral the affected peroxin is to the biogenesis and function of the peroxisome, the more severe the resulting phenotype (Argyriou et al., 2016). For example, mutations in PEX3 or PEX19, which are essential for peroxisome membrane assembly, cause severe phenotypes (Fujiki et al., 2020; Muntau et al., 2000). Many PBDs cause retinal degeneration and blindness, but precise disease mechanisms remain unknown. Our lab previously identified a patient with compound heterozygous mutations in *PEX6* causing a relatively mild systemic phenotype but prominent retinal degeneration (Benson et al., 2021). Additionally, mutations in *PEX1* are frequently associated with retinopathy (Barillari et al., 2020; Ventura et al., 2016). Mutations impairing the function of peroxisomal enzymes or peroxisome substrate transporters can also result in diseases with similar clinical manifestations to PBDs (Waterham et al., 2016).

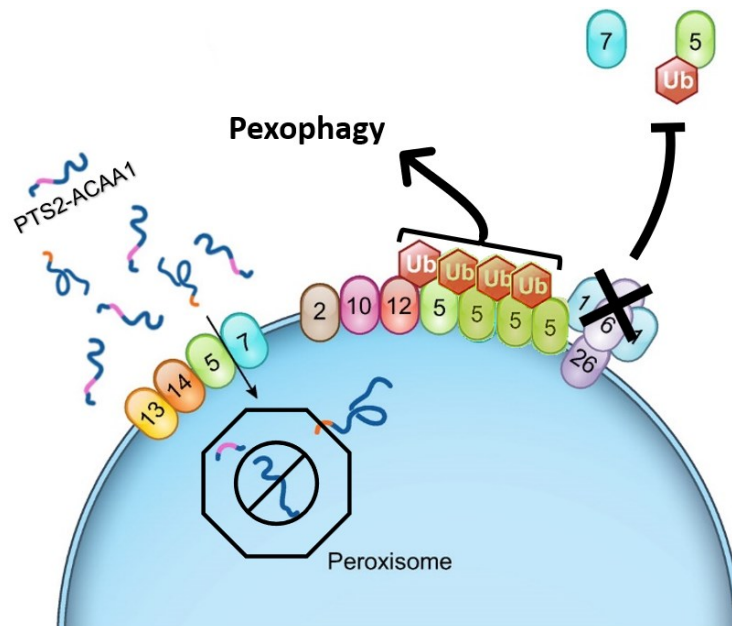


Figure 2. Consequences of PEX1 or PEX6 dysfunction on peroxisome abundance and activity. The numbered oval shapes represent peroxin proteins. Peroxisomal matrix protein import is hindered because peroxisomes no longer recycle monoubiquitinated PEX5 for subsequent rounds of matrix protein import. Instead, the accumulation of ubiquitinated PEX5 induces pexophagy. Adapted from Wanders et al., 2023.

1.4 Photoreceptors

Photoreceptors are highly specialized sensory cells that detect light through photopigment-laden discs housed in their outer segments. These sensory endings are exposed to highly oxidizing conditions that necessitate complete outer segment renewal approximately every 10 days in mammals (Kevany & Palczewski, 2010; Young, 1967). The composition of photoreceptor outer segments (POS) is well characterized, including its unique lipid content (Goldberg et al., 2016). In addition to proteins, a mosaic of lipid species contributes to the organization of POS discs including cholesterol. Long and unsaturated fatty acids offer fluidity at the central region. In contrast, short and saturated fatty acids offer membrane rigidity at the rim region (Lewandowski et al., 2022). DHA, a

long-chain polyunsaturated fatty acid product of peroxisomes, accounts for 50% of the phospholipid side chains in POS (Swinkels & Baes, 2023). VLCFAs make up to 30% of the side chains in POS (Daniele et al., 2019; Fliesler & Anderson, 1983). POS face the apical side of the retinal pigment epithelium (RPE), which ingest and metabolize aged POS (Umapathy et al., 2023; Young & Bok, 1969). In the absence of support from the neighbouring RPE, photoreceptors undergo degeneration. POS phagocytosis by the RPE enables the degradation of POS lipids and proteins (Kwon & Freeman, 2020). In particular, the ingested lipid load of POS contains substrates preferably metabolized by peroxisomes (VLCFAs), suggesting an important role for this organelle in the RPE (Figure 3).

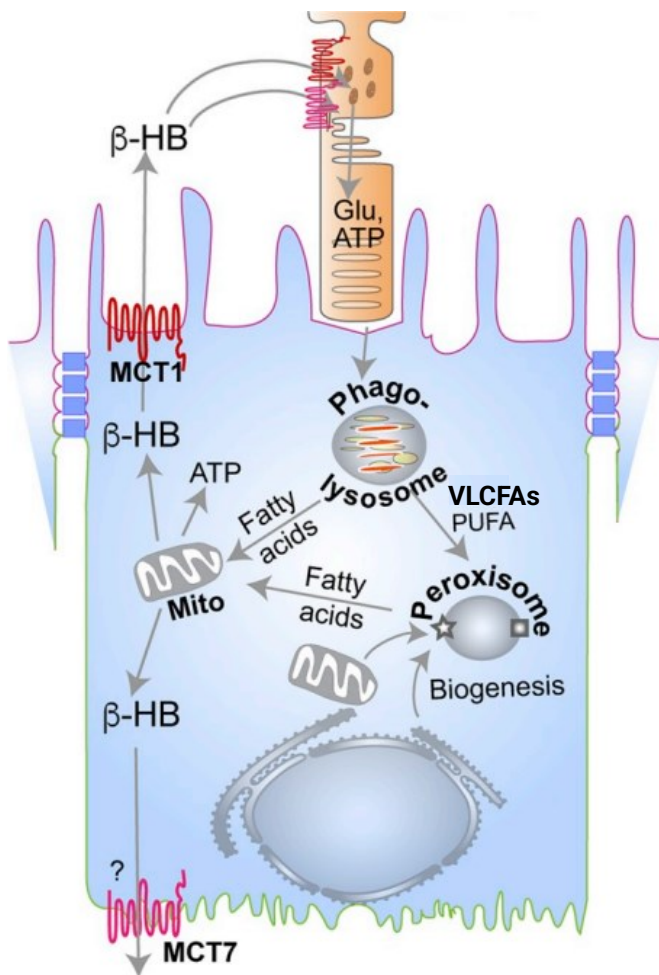


Figure 3. Anatomical relationship between a retinal pigment epithelial (RPE) cell and the apical side of a photoreceptor cell. Following POS phagocytosis, peroxisomes oxidize POS-derived VLCFAs and polyunsaturated fatty acids (PUFA). β -hydroxybutyrate (β -HB) is transported via monocarboxylate transporters (MCT). Adapted from Lakkaraju et al. Progress in Retinal and Eye Research 2020

1.5 Retinal Pigment Epithelium

The RPE interdigitates with photoreceptors and lines the back of the retina (Lakkaraju et al., 2020; Strauss, 2005). The RPE is a polarized monolayer and provides photoreceptors with glucose and recycled visual cycle element 11-cis-retinal (Fu et al., 2021). The RPE oxidizes fatty acids to satisfy intracellular energy demands, while facilitating the transfer of glucose from the bloodstream to the neural retina (Kanow et al., 2017; Sinha et al., 2020; Swarup et al., 2019). The epithelium secretes extracellular matrix components basolaterally, and contains basolateral ion channels that promote active fluid transport. This latter process may be appreciated in cell culture where basal pumping can create focal detachments of the RPE from the culture vessel (Caceres & Rodriguez-Boulan, 2020; Dvoriashyna et al., 2020). A critical role of the RPE is the phagocytosis of POS (Figure 3). In mammals, the RPE engulfs approximately 10% of POS daily, with some RPE cells handling up to 30 photoreceptors simultaneously (Kwon & Freeman, 2020; Lakkaraju et al., 2020). Lipids account for half of the internalized POS content, while proteins account for the remainder (Fliesler & Anderson, 1983). Normal handling of the ingested lipid content is crucial for the proper breakdown of the ingested proteins (Bullock et al., 2021). Vision loss may occur due to primary photoreceptor cell death or RPE cell death which secondarily leads to photoreceptor cell death. One indicator of RPE disease is the accumulation of lipofuscin – lysosomal storage bodies that form in part due to the mishandling of ingested POS (Escreveinte et al., 2021). Accumulation of apical or basal lipid-containing deposits at the level of the RPE is a precursor to RPE atrophy. Uncovering the origin of these lipid-containing deposits offers an opportunity for therapeutic intervention. Therefore, studying RPE biology in cell culture provides a model for studying RPE-autonomous defects that contribute to the formation of these deposits. RPE differentiated from induced pluripotent stem cells (iRPE) recapitulates physiological features of native RPE (Blenkinsop et al., 2015). In addition, iRPE expresses signature proteins that, in combination, are unique to RPE including: 1) tyrosinase-related protein 1 (TYRP1), an enzyme involved in RPE melanin synthesis (Gargiulo et al., 2011; Sarangarajan & Boissy, 2001), 2) paired box 6 (PAX6), a transcription factor indicative of

committed RPE that also supports melanogenesis (Raviv et al., 2014), 3) premelanosome protein (PMEL17), a transmembrane glycoprotein that supports melanogenesis in RPE (Lahola-Chomiak et al., 2019), 4) bestrophin 1 (BEST1), a calcium-dependent anion channel that localizes at the basal membrane of RPE cells (Hartzell et al., 2008; Marmorstein et al., 2000), and 5) microphthalmia-associated transcription factor (MITF), a master regulator of pigmented cells that is essential for RPE differentiation (Capowski et al., 2014).

1.6 Lipid Droplets

While melanosomes in the RPE absorb stray light to minimize oxidative stress to neighbouring cells, other organelles such as lipid droplets (LDs) support lipid homeostasis. In the RPE, the lipid content of ingested POS is incorporated into LDs. Radioactive POS-labeled DHA and arachidonic acid (C20:4n6) have been demonstrated to induce the production of triglycerides (TG) in frog RPE (Chen & Anderson, 1993). LDs are dynamic organelles that house neutral lipids, mainly TG and sterol esters. LDs are primed after the local accumulation of TG at the ER membrane. Proteins help release LDs from the ER to the cytosol (Henne et al., 2018; Zadoorian et al., 2023). Accumulation of LDs is associated with diseases that include obesity (Zimmermann et al., 2004), diabetes (Borén et al., 2013), and atherosclerosis (Perrotta, 2017). Lipolysis or lipophagy facilitates the breakdown of LDs (Fader Kaiser et al., 2022; Thelen & Zoncu, 2017). Interestingly, peroxisomes interact with LDs and may regulate lipolysis (Ding et al., 2021). Peroxisomes import and oxidize fatty acids released from LDs (Chang et al., 2019). Additionally, the peroxisomal shuttling protein, PEX5 binds and delivers a lipase to LDs (Kong et al., 2020). The presence of perilipin 2 (PLIN2), a protein that exclusively localizes to the surface of LDs (Sztalryd & Brasaemle, 2017), helps differentiate LDs from other lipid-containing deposits such as lipofuscins.

1.7 Lipid Metabolism in the Retinal Pigment Epithelium

The RPE is subject to massive lipid influx that could be highlighted as a burden or an opportunity. In a phagocytosis-dependent manner, the RPE metabolizes the ingested lipid-rich POS and releases ketone bodies back to the photoreceptors for energy (Figure 3) (Adijanto et al., 2014; Reyes-Reveles et al., 2017). Moreover, the RPE oxidizes fatty acids from internalized POS to produce energy to support its own cellular processes (Nolan et al., 2021). Importantly, normal peroxisome function is essential for RPE phagocytosis and lipid homeostasis (Das et al., 2021; Kocherlakota et al., 2023). In contrast, RPE-autonomous lipid handling defects cause the accumulation of intracellular LDs (Farnoodian et al., 2022). The presence of LDs reduces the RPE's phagocytic capacity (Yako et al., 2022). Reduction or absence of RPE phagocytosis results in photoreceptor degeneration as exemplified by mutated or absent Mer tyrosine kinase receptor (MERTK), an essential protein for phagocytosis cascade initiation in the RPE (Lukovic et al., 2015). Improper handling of the internalized POS load is invariably detrimental to the RPE.

1.8 Role of Peroxisomes in the Retinal Pigment Epithelium

Genetically mild PBD patients often present with severe retinopathy as exemplified by a patient with *PEX6* compound heterozygous mutations (Benson et al., 2021; Fujiki et al., 2020). Peroxisomes have a critical role in RPE metabolism. The POS burden that the RPE metabolizes contains VLCFAs that must be first oxidized by peroxisomes. Peroxisome activity in the RPE follows a diurnal schedule similar to that of POS phagocytosis (Daniele et al., 2019). Peroxisome proliferator activated receptor- α , a nuclear receptor that induces peroxisome generation, is essential for promoting lipid metabolism and satisfying energy demands in the retina (Pearsall et al., 2017). An accumulation of VLCFAs induce oxidative stress through lipid peroxidation (Baarine et al., 2012). Peroxisomes may protect the RPE from the toxic accumulation of peroxidated VLCFAs (Ali et al., 2023; Lu et al., 2022). When a central enzyme of the peroxisomal β -oxidation

pathway is knockedout (β -oxidation multifunctional protein 2), the RPE degenerates in mice (Das et al., 2021). Intriguingly, when the same mouse model is genetically manipulated to prevent POS formation, the RPE is rescued, presumably because of the eliminated POS load on the RPE (Kocherlakota et al., 2023). Thus, peroxisomes are clearly implicated in RPE lipid metabolism and biology. However, precisely how peroxisome dysfunction contributes to diseased RPE in PBDs remains to be fully explored.

1.9 Hypothesis

PEX1 and *PEX6* knockout iRPE were hypothesized to have defective peroxisome matrix protein import secondary to disrupted exportomer complex activity. Peroxisome abundance was hypothesized to be reduced because of the subsequent accumulation of monoubiquitinated PEX5 on the peroxisome membrane which triggers pexophagy (Figure 2). Finally, *PEX1* and *PEX6* KO iRPE challenged with POS were hypothesized to accumulate lipid relative to wild-type cells due to the impaired import of peroxisomal enzymes required for lipid catabolism.

2. Methods

2.1 Cell Culture

All cells were incubated at 37°C and 5% CO₂ in a Heracell VIOS 160i incubator (Thermo Scientific, Cat. No. 51033546). Matrix-coated culture dishes were prepared using Matrigel (Corning, Cat. No. 354234) that was diluted 1:100 in DMEM/F12 (Thermo Scientific, Cat. No. 11330032) using prechilled vessels and then applied over Nunc™ plastic cell culture dishes (Thermo Scientific, Cat. No. 140675) for one hour at room temperature. The Matrigel solution was removed before seeding cells. Cells were preserved using CryoStor® CS10 (StemCell Technologies, Cat. No. 07930, Canada). CoolCell (Corning, Cat. No. CLS432004) was used for overnight storage at -80°C to facilitate cryopreservation.

Induced Pluripotent Stem Cells (iPSCs): Gibco episomal hiPSC (wild-type) cells (Thermo Scientific, Cat. No. A18945) and isogenic *PEX1* KO (knockout), and *PEX6* KO iPSCs (Synthego, United States) were cultured in TeSR™-E8™ media (StemCell Technologies, Cat. No. 05990, Canada). Media was changed 6 days per week and doubled in volume for the 6th day. A final concentration of 10µM Y-27632 (StemCell Technologies, Cat. No. 72304, Canada) was added to the iPSC cell culture media for the first day post-thaw to improve survival (Li et al., 2008). ReLeSR™ (StemCell Technologies, Cat. No. 100-0484, Canada) enzyme-free stem cell passaging reagent was used for passaging the cells.

Induced Pluripotent Stem Cells – Retinal Pigment Epithelium cells (iRPE): The cells were generated by differentiating iPSCs. iRPE were cultured in Minimal Essential Medium α (Thermo Scientific, Cat. No. 41061029) supplemented with 2% fetal bovine serum (Millipore Sigma, Cat. No. F1051), 2% KnockOut serum replacement (Thermo Scientific, Cat. No. 10828028), 1x non-essential amino acids (Cytiva, Cat. No. SH3023801 -100x), 1x penicillin/streptomycin (Cytiva, Cat. No. SV30010 -100x), 0.5x N-2 supplement (Thermo Scientific, Cat. No. 175020DPBS48 -100x), 250µg/ml taurine (Sigma Aldrich, Cat. No. T8691-25G) dissolved in Dulbecco's Phosphate Buffered Saline (DPBS) (Cytiva, Cat. No.

SH30028.02), 14pg/ml triiodo-L-thyronine (Sigma Aldrich, Cat. No. T5516), and 20ng/ml hydrocortisone (Sigma Aldrich, Cat. No. H0888). The formulation was derived from a published protocol (Sharma et al., 2022). Media changes were performed once every 2 days. A final concentration of 10 μ M Y-27632 was added to the iRPE media for the first two days post-thaw. iRPE were passaged three times at most using TrypLE™ (Thermo Scientific, Cat. No. 12563011). Cells were cultured as follows: 1) on Matrigel-coated 60mm dishes (Thermo Scientific, Cat. No. 130183) for downstream mass spectrometry analysis, 2) on 12mm transwells (Corning, Cat. No. 3460) for downstream flow cytometry analysis and imaging, 3) on 6.5mm transwells (Corning, Cat. No. 3470) for transepithelial resistance monitoring, 4) on glass bottom chamber slides (ibidi, Cat. No. 80827, Germany) for basal imaging, and 5) on removable chamber slides (Sarstedt, Cat. No. 946170802, Germany) for apical imaging.

2.2 Generating iRPE (Induced Pluripotent Stem Cells to Retinal Pigment Epithelium)

The wild-type, *PEX1* KO, and *PEX6* KO iPSCs were differentiated simultaneously. iPSCs were passaged 3 times using ReLeSR™ before seeding uniform colonies for differentiation in TeSR™-E8™ medium supplemented with 2.5 μ M blebbistatin (SigmaAldrich, Cat. No. B0560) to promote iPSC survival (Ohgushi et al., 2010; Walker et al., 2010; Xu et al., 2010). Following this, TeSR™-E8™ medium without blebbistatin was used until the cells reached 70% confluency. Differentiation then commenced (Figure 4, Day 0) via incubating the cells with differentiation media as outlined below:

iPSC-RPE differentiation media was derived from (Regent et al., 2019): HyClone Dulbecco's Modified Eagle Medium (DMEM) with high glucose (Cytiva, Cat. No. SH30243.01) supplemented with 1x non-essential amino acids (Cytiva, Cat. No. SH3023801 -100x), and 20% KnockOut serum (Thermo Scientific, Cat. No. 10828028). The media was filtered through a 0.2 μ m pore size vacuum filter (Thermo Scientific, Cat. No. 568-0020). The media was changed 3 times per week. At each media change, 50 μ M

of 2-mercaptoethanol (BioRad, Cat. No. 1610170) was added to sequester reactive oxygen species.

For the first week, 10mM nicotinamide (StemCell Technologies, Cat. No. 07154) was added to the medium between Day 0 and Day 7 (Figure 4). Nicotinamide induces iPSCs to exit their pluripotent state and promotes the expression of early eye field transcription factors like retina and anterior neural fold homeobox (RAX) (Regent et al., 2019). For the second week, 100ng/ml Activin-A (StemCell Technologies, Cat. No. 78001) was added to the medium between Day 7 and Day 14 (Figure 4). Activin A, a member of the transforming growth factor β family, promotes optic vesicle patterning by inducing the expression of MITF (Regent et al., 2019). For the following 4 weeks, 3 μ M CHIR99021 (StemCell Technologies, Cat. No. 72054) was added to the medium between Day 14 and Day 42 (Figure 4). CHIR99021 is a glycogen synthase kinase 3 inhibitor which activates Wnt signalling and promotes commitment to an RPE fate. At Day 42 (Figure 4), the cells were washed once with DPBS then incubated with TrypLE™ for 10 minutes at 37°C and 5% CO₂, and then the media was discarded. The cells were collected after a second TrypLE™ incubation of 20 minutes. Differentiation media was added to dilute the TrypLE™. The cells were centrifuged for 5 minutes at 300g. After decanting the diluted TrypLE™ solution, the cells were resuspended in a 1:1 mixture of differentiation media: iRPE media that was topped up to a final concentration of 1x penicillin/streptomycin, and supplemented with 10 μ M Y-27632. Cells were passed through a 16G needle (Becton Dickinson, Cat. No. 305198) and then a 40 μ m strainer (Sarstedt, Cat. No. 83.3945.040, Germany) to dissociate the population to single cells. Cells were seeded at 300,000 cells per cm² and then incubated undisturbed for 2 days. Cells were cultured for 3 additional weeks in iRPE media as indicated by the arrow between Day 42 and Day 62 (Figure 4). Afterwards, cells were similarly washed once with DPBS and were then subjected to a primary and a secondary TrypLE™ incubation. Likewise, cells were seeded at 300,000 cells per cm² with iRPE media supplemented with 10 μ M Y-27632. Cells were cultured with iRPE media from the second media change onwards. The cells were considered mature 3 weeks after their

last seeding. Alternatively, cells were seeded and cultured for a few days before cryopreservation (Zhang et al., 2022).

2.3 DNA Sanger Sequencing

DNA was isolated from iRPE using GeneJET Genomic DNA Purification Kit (Thermo Scientific, Cat. No. K0722) and eluted in molecular grade water. DNA concentration was determined using a μ Drop™ plate (Thermo Scientific, Cat. No. N12391) and Multiskan™ GO Microplate Spectrophotometer (Thermo Scientific, Cat. No. 51119300). Polymerase chain reactions (PCR) were performed as outlined below to amplify DNA regions of interest.

A 1% agarose (Thermo Scientific, Cat. No. 16500500) gel was prepared with TAE (Tris-acetate-ethylenediaminetetraacetic acid) buffer. SYBR™ Safe (Thermo Scientific, Cat. No. S33102) was added before gel solidification. PCR products supplemented with loading dye (Thermo Scientific, Cat. No. R0611) and GeneRuler 1kb ladder (Thermo Scientific, Cat. No. SM1331) were subjected to gel electrophoresis at 150V for 40 minutes. The resulting gel was visualized with ultraviolet light. Gel areas of interest were excised and DNA was purified using QIAquick Gel Extraction Kit (QIAGEN, Cat. No. 28706). Sanger sequencing was performed at the Molecular Biology Service Unit at the University of Alberta.

2.3.1 PEX1 Knockout Validation

50 μ L PCR reactions were performed using Taq DNA polymerase (New England Biolabs, Cat. No. M0273L). Forward (5'-GAACTCTTTTTGGACATGTGAATTG-3') and reverse (5'-GCAAGTAGGGAGTATGGTAAACT-3') primers were used at 0.2 μ M. dNTPS (Thermo Scientific, Cat. No. 10297018) were used at a concentration of 10mM. Reactions were subject to one denaturation step for 30 seconds at 95°C, followed by 30 cycles of 22

seconds duration at 95°C, 15 seconds at 49°C, and 27 seconds at 68°C, followed by one extension step for 5 minutes at 68°C.

2.3.2 PEX6 Knockout Validation

50µL touchdown PCR reactions were performed using Phusion DNA polymerase and GC buffer (Thermo Scientific, Cat. No. F534S). Forward (5'-AGAAACCGCAAAGGAGGAC-3') and reverse (5'-ACTAGTCGTCTGGCTCTCTG-3') primers were used at a concentration of 0.2µM. dNTPS (Thermo Scientific, Cat. No. 10297018) were used at 10mM. Reactions were subject to one denaturation step for 30 seconds at 98°C, followed by 10 touchdown cycles of 10 seconds at 98°C, 20 seconds at 66°C (decreasing by 0.5°C each cycle), and 21 seconds at 72°C. This was followed by 25 cycles of 30 seconds at 98°C, 20 seconds at 61°C, and 21 seconds at 72°C, followed by one extension step for 5 minutes at 72°C.

2.4 Western Blotting

Cell culture media was removed by aspiration, cells were washed once with DPBS. Then, 20µL per cm² of cold radioimmunoprecipitation (RIPA) buffer (Thermo Scientific, Cat. No. 89900) supplemented with cOmplete™ Protease Inhibitor Cocktail (Sigma Aldrich, Cat. No. 11697498001) was applied to the cells which were then incubated on ice for 3 minutes. Cells were harvested by mechanical scraping and transferred to Eppendorf tubes and then incubated on ice for 15 minutes. Lysates were obtained by sonicating cells for 10 seconds at 5% output (Branson Sonifier 450) and cleared lysates were obtained by centrifugation for 15 minutes at 16,000g at 4°C. The supernatant was subsequently collected.

Protein concentration was determined using Pierce™ BCA Protein Assay Kit (Thermo Scientific, Cat. No. 23225). Multiskan™ GO Microplate Spectrophotometer (Thermo Scientific, Cat. No. 51119300) was used to measure absorbance at 562 nm.

Protein samples were diluted with RIPA buffer supplemented with the protease inhibitor cocktail to reach a desired amount of protein (10µg-50µg) to load on SDS-PAGE gels. Samples were mixed with 1x Laemmli Sample Buffer (Bio-Rad, Cat. No. 1610747 – 4x) supplemented with freshly added 20% 2-mercaptoethanol (Sigma Aldrich, Cat. No. M3148). A final concentration of 5% of 2-mercaptoethanol was achieved. Samples were incubated at 70°C for 10 minutes and then centrifuged at 2600g to facilitate sample collection and gel loading. Samples were loaded onto 4-15% Mini-PROTEAN® TGX™ Precast Protein Gels precast (Bio-Rad, Cat. No. 4561084) housed in Mini-PROTEAN® Tetra Cell (Bio-Rad, Cat. No. 1658037) submerged with 1 L of running buffer (25 mM Tris, 190 mM glycine, 0.1% SDS). Gels loaded with protein samples and Chameleon™ Duo pre-stained protein ladder (Li-Cor, Cat. No. 928-60000) were subject to 100V for 120 minutes (Bio-Rad PowerPac™ Basic Power Supply). Following electrophoresis, proteins were transferred to a nitrocellulose membrane (Thermo Scientific, Cat. No. IB23002) using 23V for 6 minutes with the iBlot™ 2 dry blotting system (Thermo Scientific, Cat. No. IB21001). Membranes were protected from light and incubated with Intercept® PBS Blocking Buffer (Li-Cor, Cat. No. 927-70001) for 1 hour at room temperature. All incubations and washes were performed on a rocker. Tween-20 0.05% (Bio-Rad, Cat. No. 1706531) was added to PBS to create PBS-T. A 1:1 blocking buffer:PBS-T solution was prepared to dilute antibodies for incubations. Primary antibodies (Table 1) were applied overnight at 4°C. After the incubation, membranes were washed with PBS-T thrice for 5 minutes each. Secondary antibodies (Table 1) were applied for 1 hour at room temperature. Following the incubation, membranes were washed with PBS-T twice for 10 minutes each and then once with PBS for 10 minutes.

Membranes were scanned using the Odyssey CLx imaging system (Li-Cor) and visualized on Image Studio (LiCor, V.5.2). Blots were captured with a high-quality setting at 169µm resolution. Regions of interest were manually selected and raw intensity values were recorded. Values were adjusted using their respective loading controls and then normalized to the wild-type using Microsoft® Excel® (Version 2401 Build 16.0.17231.20236).

2.5 Immunofluorescence

This protocol was derived from Listenberger et al., 2016. Cells were prepared using the same protocol regardless of the culture vessel. A solution made of PBS supplemented with 0.1% saponin (Millipore Sigma, Cat. No. 558255) and 1% bovine serum albumin (Sigma Aldrich, Cat. No. A9418) was used to block and dilute antibodies for incubations.

After decanting the media, cells were washed once with DPBS. Cells were then incubated on ice with 4% paraformaldehyde (Sigma Aldrich, Cat. No. P6148-500G) for 15 minutes. The solution was decanted, and cells were washed 3 times with DPBS. Cells were blocked for 30 minutes with Intercept® (PBS) Blocking Buffer (LiCor, Cat. No. 927-70001) at room temperature, and then incubated with primary antibodies for 1 hour at room temperature, or directly incubated with primary antibodies for 30 minutes at 37°C if BODIPY was used. Cells were then washed 3 times with DPBS, and then incubated with secondary antibodies at room temperature for 1 hour, or 30 minutes if BODIPY was previously applied. Cells were again washed 3 times with DPBS, and then incubated with 1.67µM DAPI (Millipore Sigma, Cat. No. D8417) for 5 minutes at room temperature. Cells were finally washed 3 times with DPBS. ProLong™ Diamond Antifade Mountant (Thermo Scientific, Cat. No. P36970) was applied before placing #1.5 coverslips (Fisherbrand, Cat. No. 12541B) on the slides. The slides were left to dry at room temperature overnight, protected from light.

To quantify PMP70 positive puncta, images were captured using the Zeiss 510 META laser scanning confocal microscope at the Cell Biology Imaging Facility at the University of Alberta. A 63X objective lens was used. Three independent wells of each cell line were imaged using the same settings. Captured z-stacks were analysed using IMARIS (Oxford Instruments, V. 10.1). A fellow graduate student (Ehsan Misaghi) blinded the images by generating a set of random numbers for each pair of images. He then imported all the images within the folder and changed their names, taking into account the pair they belonged to. He saved the original and blinded names onto a spreadsheet. The analysis was done on blinded images, and the results were saved using the random numbers associated with each image and its pair. The generated spreadsheet was then used to

change the names of the analyzed files back to the original name before statistical analysis. The spots detection tool was employed with a $0.3\mu\text{m}$ diameter parameter to automatically detect PMP70 positive puncta. Cell borders were manually drawn using the Draw tool. The outlined cell area was placed at the most apical and basal layers, and then used to generate a surface, effectively creating a 3D cell volume. The filter tool was used to determine the number of spots inside each cell by selecting all spots that were less than $0\mu\text{m}$ away from the cell's 3D surface. Relative to the cell's surface, intracellular spots had a negative distance. The number of spots per cell and the corresponding cell volume were recorded. There were 385 cells analyzed in total. The number of spots was normalized against the corresponding cell volume. These values were multiplied by a constant, which was the pooled average volume of each iRPE cell line. Data was managed using Microsoft® Excel® (Version 2401 Build 16.0.17231.20236).

All other images were captured using the Leica TCS SP5 Laser Scanning Confocal Microscope at the Cell Imaging Core at the University of Alberta or the Leica THUNDER - Deconvolution Widefield Microscope, both with a 100x objective lens. Maximum intensity projections were developed using ImageJ (NIH, V1.53t). Images were edited by linearly adjusting white and black levels using Affinity Photo 2 (Serif, V2.30).

2.6 Flow Cytometry

The protocol was derived from Qiu & Simon, 2016. Suitable gating strategies and other technical aspects of flow cytometry were developed in consultation with the University of Alberta Flow Cytometry Core Facility (Dr. Aja Reiger). A minimum of 10,000 events were collected for each sample. Data were analyzed using FlowJo v10.10.0 (BD Biosciences). Cells were gated based on the FSC/SSC (forward scatter/ side scatter) profile to exclude debris and cell clumps. FSC area versus FSC height was then used to remove doublets. Single cells were gated based on fluorescence minus one (FMO) controls. These cells were then analyzed based on the % gated as well as the median and mean fluorescence intensity.

To determine iRPE population heterogeneity, antibodies against 5 proteins expressed in mature iRPE were captured via two panels. Fixed iRPE were run on a 5 laser Cytex Aurora (Cytex Biosciences) flow cytometer. Samples acquired on the Aurora were unmixed with autofluorescence subtraction using single-stained reference controls. First, the cells were washed with DPBS. Next, TrypLE™ was applied for 30 minutes until the cells detached. Cells were then pelleted by centrifugation at 300g for 5 minutes. The solution was discarded, and cells were resuspended in flow cytometry buffer made of DPBS supplemented with 2% fetal bovine serum (Sigma Aldrich, Cat. No. F1051-500ml). Then, 10µl from the resuspended solution was mixed with 10µl of Trypan Blue (HiMedia, Cat. No. TCL005-100ml) to count cells using the Countess 3 (Thermo Scientific, Cat. No. AMQAX2000). Cells were pelleted again, then resuspended with 4% formaldehyde and incubated at room temperature for 15 minutes. Five volumes of flow cytometry buffer were added before the cells were centrifuged at 400g for 4 minutes. The supernatant was discarded, and the cells were resuspended in the flow cytometry buffer and separated into Eppendorf tubes, each containing 500,000 cells. Cells were centrifuged at 400g for 4 minutes, and then the supernatant was discarded. Cells were resuspended in a permeabilization buffer containing flow cytometry buffer supplemented with 0.2% Triton X-100 (Bio-Rad, Cat. No. 1610407) that included the primary antibodies. Cells were incubated overnight at 4°C on a rocker. The following day, cells were washed with 2 volumes of flow cytometry buffer, and then centrifuged at 400g for 4 minutes. After discarding the supernatant, cells were resuspended with the permeabilization buffer supplemented with the secondary antibodies. Cells were incubated at room temperature for 30 minutes on a rocker. After, cells were washed with 2 volumes of flow cytometry buffer and then centrifuged at 400g for 5 minutes. The supernatant was subsequently discarded. The cells were incubated in flow cytometry buffer containing 1.67µM DAPI (Millipore Sigma, Cat. No. D8417) for 5 minutes at room temperature. After, cells were washed with 2 volumes of flow cytometry buffer and then centrifuged at 400g for 5 minutes. The supernatant was subsequently discarded. Finally, cells were resuspended in flow cytometry buffer and run on the flow cytometer.

To quantify BODIPY 493/503 mean fluorescent intensity changes after feeding iRPE with 10 POS/cell for 7 consecutive days, live iRPE were run on a 4 laser Attune NxT (ThermoFisher Scientific; blue/red/yellow/violet 6 configuration). Samples acquired on the Attune NxT were compensated using single-stained controls. Experimental cells were first washed with DPBS after aspirating the culture media. Then, cells were incubated with media supplemented with 2 μ M BODIPY 493/503 (Fisher Scientific, Cat. No. D3922) and 5 μ g/ml Hoechst (Thermo Scientific, Cat. No. 33342) for 30 minutes at 37°C. Following this incubation, cells were washed with DPBS, and then TrypLE™ was applied for 30 minutes until the cells detached. TrypLE™ was diluted with DPBS and then cells were centrifuged for 5 minutes at 300g. The supernatant was discarded, and cells were resuspended in the flow cytometry buffer and run on the flow cytometer.

2.7 Mass Spectrometry

Mature wild-type and *PEX6* KO iRPE cultured on 60mm dishes were used for this experiment. Three replicates were analyzed for each cell line. To harvest the cells, each cell culture dish was washed with DPBS (Thermo Scientific, Cat. No. 14190144), and then incubated with 2ml of TrypLE™ (Thermo Scientific, Cat. No. 12563011). Once the cells detached, TrypLE™ was further diluted with DPBS. Cells were centrifuged at 300g for 5 minutes (Thermo Scientific, Cat. No. 05-413-310). After decanting the diluted TrypLE™ solution, the cell pellet was resuspended in 5mL of DPBS. Then, 10 μ L from the 5mL solution was mixed with 10 μ L of Trypan Blue (HiMedia, Cat. No. TCL005-100mL) to count cells using the Countess 3 (Thermo Scientific, Cat. No. AMQAX2000). The total number of cells was recorded. The cells were pelleted again by centrifugation at 300g for 5 minutes. After decanting the DPBS, the cells were resuspended in 1ml of DPBS and transferred to a 1.5ml Eppendorf tube (Thermo Scientific, Cat. No. 3448). The cells were centrifuged again at 300g for 5 minutes, and then the DPBS was aspirated. All of the tubes were snap-frozen by pouring liquid nitrogen over them. Finally, the samples were stored at -80°C until processing.

The following work was conducted by Creative Proteomics, NY, United States:

Samples were transferred into a screw-cap glass vial which contained tritricosanoic acid as an internal standard (tri-C23:0 TG) (NuCheck Prep, Elysian, MN). A portion of the organic layer was transferred to a screw-cap glass vial and dried in a speed vacuum. Next, BTM (methanol containing 14% boron trifluoride, toluene, methanol; 35:30:35 v/v/v) (SigmaAldrich, St. Louis, MO) was added. The vial was briefly vortexed and heated in a hot bath at 100°C for 45 minutes. After cooling, hexane (EMD Chemicals, USA) and HPLC grade water were added, the tubes were recapped, vortexed and centrifuged to help separate the layers. An aliquot of the hexane layer was transferred to a GC (Gas Chromatography) vial.

Fatty acids were identified by comparison with a standard mixture of fatty acids (GLC OQ-A, NuCheck Prep, Elysian, MN), which was also used to determine individual fatty acid calibration curves.

2.8 Photoreceptor Outer Segments Isolation

This protocol was adopted from Parinot et al., 2014. Eighty frozen bovine eyes were sourced from a local abattoir for POS isolation.

A homogenization solution (20% sucrose, 20mM tris acetate pH7.2, 2mM MgCl₂, 10mM glucose and 5mM taurine) and multiple wash solutions (20mM tris acetate pH 7.2 and then sucrose containing) were prepared as described (Parinot et al., 2014). Sucrose gradients were cast independently of each other using a gradient maker (Hoefer™ SG 100). Under red light, after thawing the eyes, an incision was made approximately 3mm posterior to the limbus of each bovine eye using a 15-degree paracentesis blade. The incision was continued circumferentially using Westcott scissors. Once the incision was completed, the corneoscleral cap was removed to expose the posterior chamber and vitreous cavity. After removing the lens and the vitreous humor, the retina was gently scraped off of the underlying retinal pigment epithelium and tapetum lucidum using a

small muscle hook. The retinas were collected in a 50ml Falcon tube containing homogenization solution and then placed on ice. Homogenization was achieved by manually agitating or shaking the tube containing the retinas for 2 minutes. The homogenized solution was then filtered twice through double-layer gauze. The filtered solution was then transferred on top of the sucrose gradients. Samples were centrifuged (Beckman Coulter, Optima L-100K Ultracentrifuge) for 2 hours at 27,000 RPM at 4°C (Beckman Coulter, SW 28 rotor). The resulting orange bands from multiple ultracentrifuge tubes (Supplementary Figure 1) were isolated and then subjected to serial washes with wash buffers 1, 2, and then 3, respectively (Parinot et al., 2014). The isolated POS were then counted using a hemocytometer, aliquoted, and resuspended in iRPE media supplemented with 2.5% sucrose. The POS were snap-frozen and then stored at -80°C.

For use in experiments, POS were thawed and then centrifuged at 2300g for 5 minutes in a swinging bucket rotor. The supernatant was decanted, and the POS were resuspended in iRPE media and then added to cultured cells (10 POS per cell).

2.9 Antibodies

Table 1. List of antibodies with corresponding application and concentration. FC = flow cytometry; WB = western blot; IF = immunofluorescence.

| Antibody | Clonality and Source | Manufacturer and Catalogue Number | Application and Dilution |
|--|----------------------|-----------------------------------|----------------------------------|
| TYRP1 | Mouse monoclonal | Novus Biologicals (32906) | FC: 1:100 (0.2mg/ml) |
| PAX6 | Rabbit polyclonal | Proteintech (12323) | FC: 1:250 (900µg/ml) |
| PMEL17 | Mouse monoclonal | Santa Cruz (377325) | FC: 1:100 (200µg/ml) |
| BEST1 | Mouse monoclonal | Santa Cruz (32792) | FC: 1:100 (200µg/ml) |
| MITF | Rabbit monoclonal | Invitrogen (32554) | FC: 1:100 (1mg/ml) |
| Goat anti Rabbit conjugated to Alexafluor 488 | Goat polyclonal | Invitrogen (A11034) | FC: 1:500 (2mg/ml) |
| Donkey anti mouse conjugated to Alexafluor 647 | Donkey polyclonal | Thermo Fisher (31571) | FC: 1:500 (2mg/ml) |
| PMP70 | Rabbit polyclonal | Abcam (ab3421) | WB: 1:1000 (1mg/ml) IF: 1:50 |
| PEX1 | Rabbit polyclonal | Proteintech (13669) | WB: 1:500 (500µg/ml) |
| PEX6 | Mouse monoclonal | Santa Cruz (sc271813) | WB: 1:50 (200µg/ml) |
| ACAA1 | Rabbit polyclonal | Abcam (ab154091) | WB: 1:1000 (1mg/ml) IF: 1:100 |
| γ-Tubulin | Mouse monoclonal | Millipore Sigma (T5326) | WB: 1:1000 (1mg/ml) |
| Goat anti mouse conjugated to IRDye 800 | Goat polyclonal | Li-Cor (926-32210) | WB: 1:5000 (1mg/ml) |
| Goat anti rabbit conjugated to IRDye 800 | Goat polyclonal | Li-Cor (926-32211) | WB: 1:5000 (1mg/ml) |
| Goat anti mouse conjugated to IRDye 680 | Goat polyclonal | Li-Cor (926-68070) | WB: 1:5000 (1mg/ml) |
| Goat anti rabbit conjugated to IRDye 680 | Goat polyclonal | Li-Cor (926-68071) | WB: 1:5000 (1mg/ml) |
| CLDN19 (Claudin-19) | Mouse monoclonal | Santa Cruz (365967) | IF: 1:10 (200µg/ml) |
| ADRP (PLIN2) | Mouse monoclonal | Santa Cruz (377429) | IF: 1:100 (200µg/ml) |
| ZO-1 | Mouse monoclonal | Thermo Fisher (339188) | IF: 1:10 (500µg/ml) |
| β-actin | Mouse monoclonal | Santa Cruz (69879) | WB: 1:500 (100µg/ml) |
| β-actin | Rabbit polyclonal | Abcam (ab8227) | WB: 1:1000 (300µg/ml) |

2.10 Statistics

PMP70 positive puncta quantification from immunofluorescence experiments and protein quantification from western blot experiments were compared by using a one-way ANOVA with $\alpha = 0.05$. Tukey's multiple comparisons test was also performed to compare groups. BODIPY 493/503 mean fluorescence intensities measured by flow cytometry were compared using a two-way ANOVA with $\alpha = 0.05$ and a Tukey's test. Fatty acid abundance, measured by GS-FID, was compared using a two-way ANOVA with $\alpha = 0.05$ and a Sidak's test. Statistical analysis was performed in GraphPad Prism version 10.0.2.

3. Results

3.1 Differentiation of Induced Pluripotent Stem Cells to Retinal Pigment Epithelium

To study the effect of peroxisome dysfunction on a disease-relevant cell type, *PEX1* KO, *PEX6* KO, and wild-type iPSCs were differentiated into RPE. At first, iPSC colonies were seeded uniformly on 6-well plates (Day -3) (Figure 4). By Day 0, confluency was almost reached. The cumulative effect of nicotinamide and activin A induced the generation of RPE progenitor cells through the upregulation of eye field lineage-specific signature proteins, including PAX6 (Regent et al., 2019; Sharma et al., 2022). The application of CHIR99021 supported RPE-fate commitment because it results in the upregulation of *MITF* (Microphthalmia-associated transcription factor), demonstrated by the increased cellular pigmentation (Regent et al., 2019). On Day 62, the cells appeared more uniform following re-plating on Day 42 after capturing images of the cells (Figure 4). Pigmentation reappeared 3-4 weeks post-seeding. All three cell lines (wild-type, *PEX6* KO, and *PEX1* KO) were differentiated effectively simultaneously and exhibited no overt morphological differences from each other on brightfield microscopy.

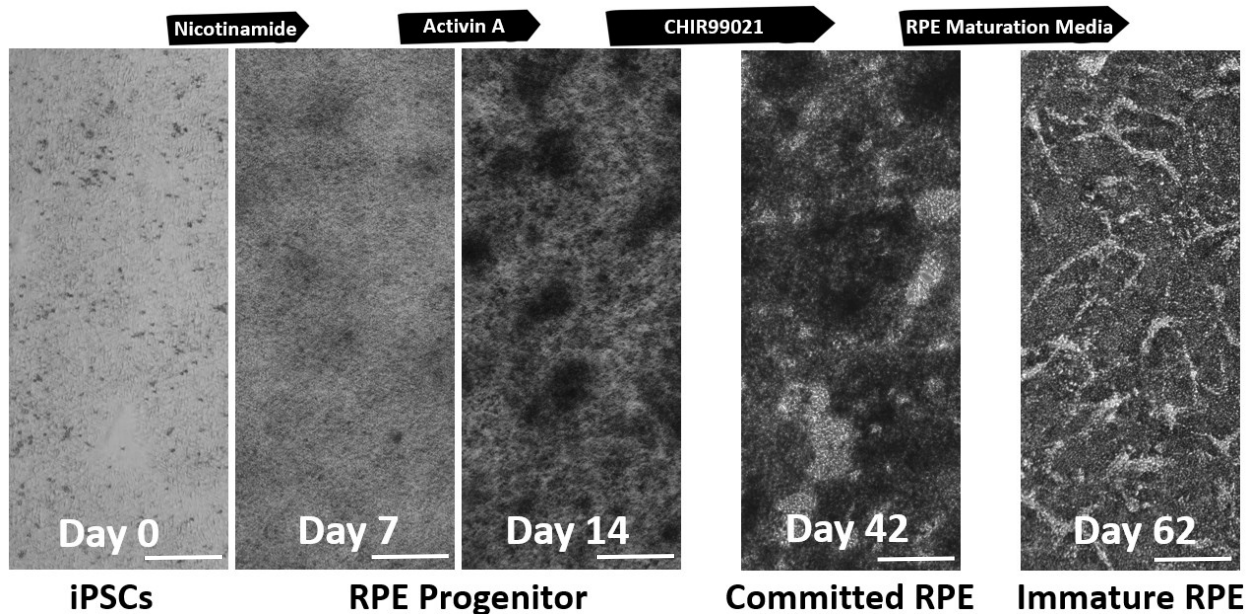


Figure 4. Differentiation stages and timeline for the conversion of iPSC to RPE. Representative brightfield images of iRPE differentiation captured using EVOS M5000 with a 4X objective lens. The black arrows at the top represent the application of the indicated supplements over the differentiation timeline. Nicotinamide was used to promote iPSC differentiation. Activin A promoted the development of RPE progenitors and CHIR99021 promoted RPE commitment. Differentiation stages are highlighted at the bottom of the images. The scale bar is 350µm.

3.2 Validation of Retinal Pigment Epithelium (iRPE)

To confirm the successful differentiation of iRPE, flow cytometry was used to detect the expression of signature proteins that, in combination, are unique to the RPE. In general, all three cell lines (*PEX1* KO, *PEX6* KO, and wild-type) were comparable and had reached a similar degree of differentiation and population homogeneity as determined by a 91% average detection of iRPE-signature proteins (Table 2). Based on positive antibody labelling of the target proteins, TYRP1 was least detected in wild-type and *PEX6* KO iRPE at 88.6% and 82.6%, respectively. PMEL17 was most abundantly expressed across all iRPE lines. The *PEX1* KO iRPE had the highest detection of all iRPE-signature proteins (Table 2).

Table 2. Detecting RPE signature proteins using flow cytometry to validate *PEX1* KO, *PEX6* KO, and wild-type iRPE. DAPI and cellular granularity (side scatter) were used to identify single cells for analysis. At least 10,000 events were captured for each sample. Two experimental flow panels were used to probe the cells.

| iRPE-Signature Protein | Wild type | <i>PEX6</i> KO | <i>PEX1</i> KO |
|------------------------|-----------|----------------|----------------|
| TYRP1 | 88.6% | 82.6% | 93.5% |
| PAX6 | 90.7% | 85.9% | 94.7% |
| PMEL17 | 92.1% | 92.4% | 93.8% |
| BEST1 | 91.5% | 91.6% | 93.5% |
| MITF | 90.4% | 90.5% | 92.8% |

Certain regions of the iRPE cell monolayer were observed detaching from the surface (Figures 5A and B), likely due to the activity of basal ion pumps and fluid channels that drive basal water movement, a feature consistent with effective RPE polarization (Dvoriashyna et al., 2020). Mature iRPE (Figure 5C) were more pigmented than immature iRPE (Figure 5B), and this increase in pigmentation was consistently apparent throughout the differentiation process (Figures 3 and 4).

Additionally, iRPE formed tight junctions as demonstrated by the presence of Claudin-19 and Zonula Occludins-1 by immunofluorescence microscopy (Figure 10 and Supplementary Figure 2). Following differentiation, *PEX1* KO, *PEX6* KO, and wild-type iRPE expressed RPE-signature proteins, developed pigment, and formed tight junctions, supporting the successful differentiation of all three cell lines to mature iRPE.

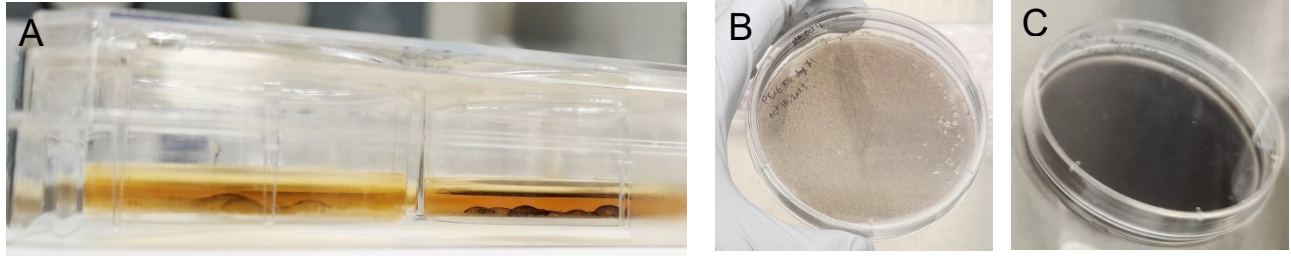


Figure 5. Pigmentation and basal fluid pumping in iRPE. A) iRPE cells captured tangentially from a 6-well plate during differentiation (day 37). B) iRPE cells maturing on a 60mm dish (day 74). C) Mature pigmented iRPE cells captured on a 60mm dish (day 95).

3.3 Evaluation of Peroxisomes in the Retinal Pigment Epithelium

3.3.1 Verification of PEX1 and PEX6 Knockouts

PEX1 and *PEX6* KO iPSCs were commercially obtained (Synthego, United States). Once the iPSCs were differentiated to iRPE, the mutations were confirmed by Sanger sequencing, and *PEX1* and *PEX6* KO was verified at the protein level by western blot. *PEX1* KO iRPE were homozygous for c.178dup; p.(W60Lfs*8) in exon 2 of 24. *PEX6* KO iRPE were homozygous for c.197dup; p.(Q67Afs*11) in exon 1 of 17 (Figure 6 A). The *PEX1* protein was detected in wild-type iRPE but was absent in the *PEX1* KO iRPE (Figure 5B). The *PEX6* protein was detected in wild-type iRPE but was absent in the *PEX6* KO iRPE (Figure 5B).

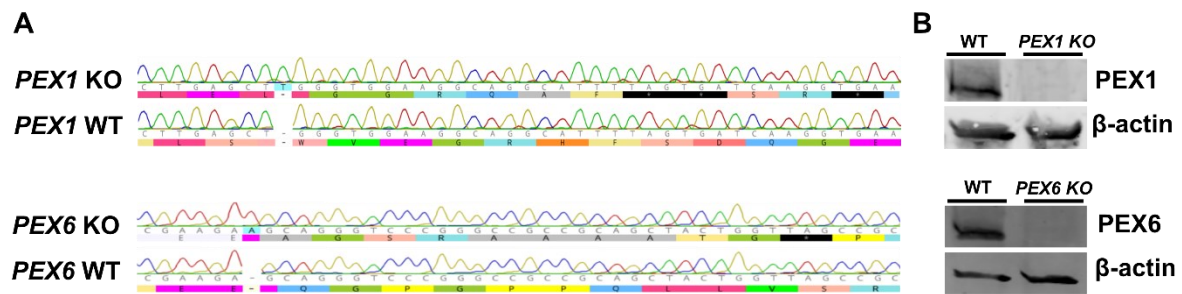


Figure 6. Confirmation of PEX1 and PEX6 knockout at the DNA and protein levels. A) Sanger sequencing of iRPE DNA. The single base pair duplication and consequent frameshift mutations are highlighted by the dash (-) in the wild-type sequences. The resulting stop codons are highlighted by the black boxes. B) Western blotting confirms the absence of PEX1 and PEX6 protein in their respective iRPE knockout cells. 50µg of protein was loaded per well (n=3 technical replicates).

3.3.2 Peroxisome Abundance

To test the hypothesis that peroxisome abundance is reduced in exportomer-deficient iRPE, the number of PMP70-positive puncta was quantified in *PEX1* and *PEX6* KO iRPE and compared to wild-type iRPE. Both KO iRPE lines had fewer PMP70-positive puncta relative to wild-type iRPE (Supplementary Figure 3). Individual data points are reported (Supplementary Figure 4). On average, wild-type iRPE had 210 PMP70-positive puncta per cell (Figure 7B). *PEX6* KO and *PEX1* KO iRPE had 155 and 162 PMP70-positive puncta per cell, respectively (Figure 7B). For statistical analysis, when independent wells are considered, there was no significant difference in the number of PMP70-positive puncta, suggesting no difference in peroxisome abundance among the 3 cell lines ($P=0.29$; n=3 technical replicates). However, when individual cells are considered, there was a significant difference in PMP70-positive puncta among the cell lines ($P<0.0001$; n=385) (Supplementary Figure 4). Similarly, western blot quantification of PMP70 in whole cell lysates demonstrated reduced levels of PMP70 in *PEX1* and *PEX6* KO relative to wild-type iRPE, but this did not reach statistical significance ($P=0.74$) (Figure 7D).

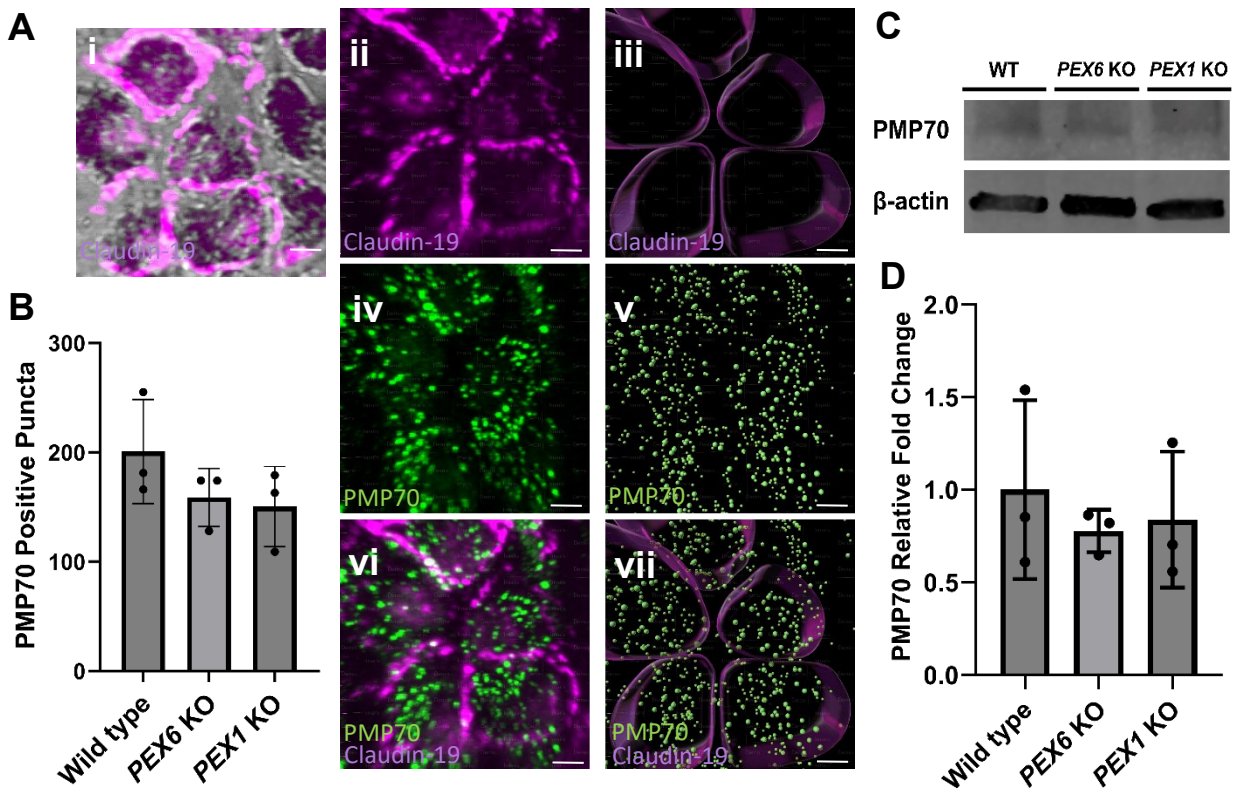


Figure 7. Quantification of PMP70-positive puncta as a measure of peroxisome abundance in iRPE. A) PMP70-positive puncta quantification of confocal microscopy images following IMARIS analysis. A(i) and A(ii) show the same iRPE border labelling using an antibody against Claudin-19. A(i) demonstrates the overlap of a brightfield image and Claudin-19 immunolabelling. A(ii), A(iv), and A(vi) demonstrate PMP70 and Claudin-19 antibody detection. A(iii), A(v), and A(vii) depict an IMARIS rendering of PMP70 (in green) using the spots function and iRPE borders (in purple) that were outlined manually. All images were acquired using a Zeiss LSM510 microscope. B) summarizes the average number of PMP70 spots detected within each identified cell border for each cell line. The data were normalized based on their respective iRPE cell volumes and were then multiplied by the average iRPE volume. Each data point corresponds to an independent iRPE culture well. There were 385 cells analyzed in total (n=3 technical replicates). Scale bar is 5µm. C) Representative immunoblot of PMP70 and β-actin

detection captured using a Li-Cor Odyssey CLx. D) Quantification of PMP70 normalized to β -actin (n=3 technical replicates). Each data point represents an independent western blot. 30 μ g of protein was loaded per well (n=3 technical replicates).

3.3.3 Peroxisomal Matrix Protein Import

To test the hypothesis that exportomer-deficient iRPE have impaired peroxisomal matrix protein import, the distribution and enzymatic processing of ACAA1 were examined. ACAA1 is targeted for peroxisomal localization by its PTS2 signal peptide (PTS-ACAA1; uncleaved) (Tsukamoto et al., 1994). Once inside the peroxisomal matrix, the PTS2 peptide is enzymatically removed (ACAA1; cleaved). PTS2-ACAA1 is 3 kDa larger than ACAA1 (Figure 8 B(i)), and this can be resolved by differential protein migration by electrophoresis. When peroxisomal import is partially disrupted, 2 bands appear on a western blot, one at 44kDa (PTS2-ACAA1) and another at 41kDa (ACAA1) (Benson et al., 2021). PTS2-ACAA1 (44kDa band) was exclusively detected in the *PEX6* KO and *PEX1* KO iRPE, suggesting impaired peroxisomal matrix protein import, whereas ACAA1 (41kDa band) was exclusively detected in wild-type iRPE, implying intact matrix import (Figure 8B (i and ii)). More replicates are presented in Supplementary Figure 5.

A predominantly punctate subcellular distribution of ACAA1 by immunofluorescence microscopy, as opposed to a diffuse cytosolic signal, implies successful peroxisomal matrix localization. ACAA1 positive puncta were most pronounced in wild-type iRPE compared to the *PEX6* KO and *PEX1* KO iRPE, where the latter KO iRPE lines exhibited a more diffuse ACAA1 signal, suggesting mislocalization and impaired matrix protein import (Figure 8 A).

Irrespective of PTS2 cleavage, total ACAA1 abundance was significantly lower in *PEX6* KO iRPE whole cell lysates relative to wild-type cells ($P=0.0058$) (Figure 8C). The amount of ACAA1 in *PEX1* KO iRPE was not significantly different than wild-type cells ($P=0.0609$).

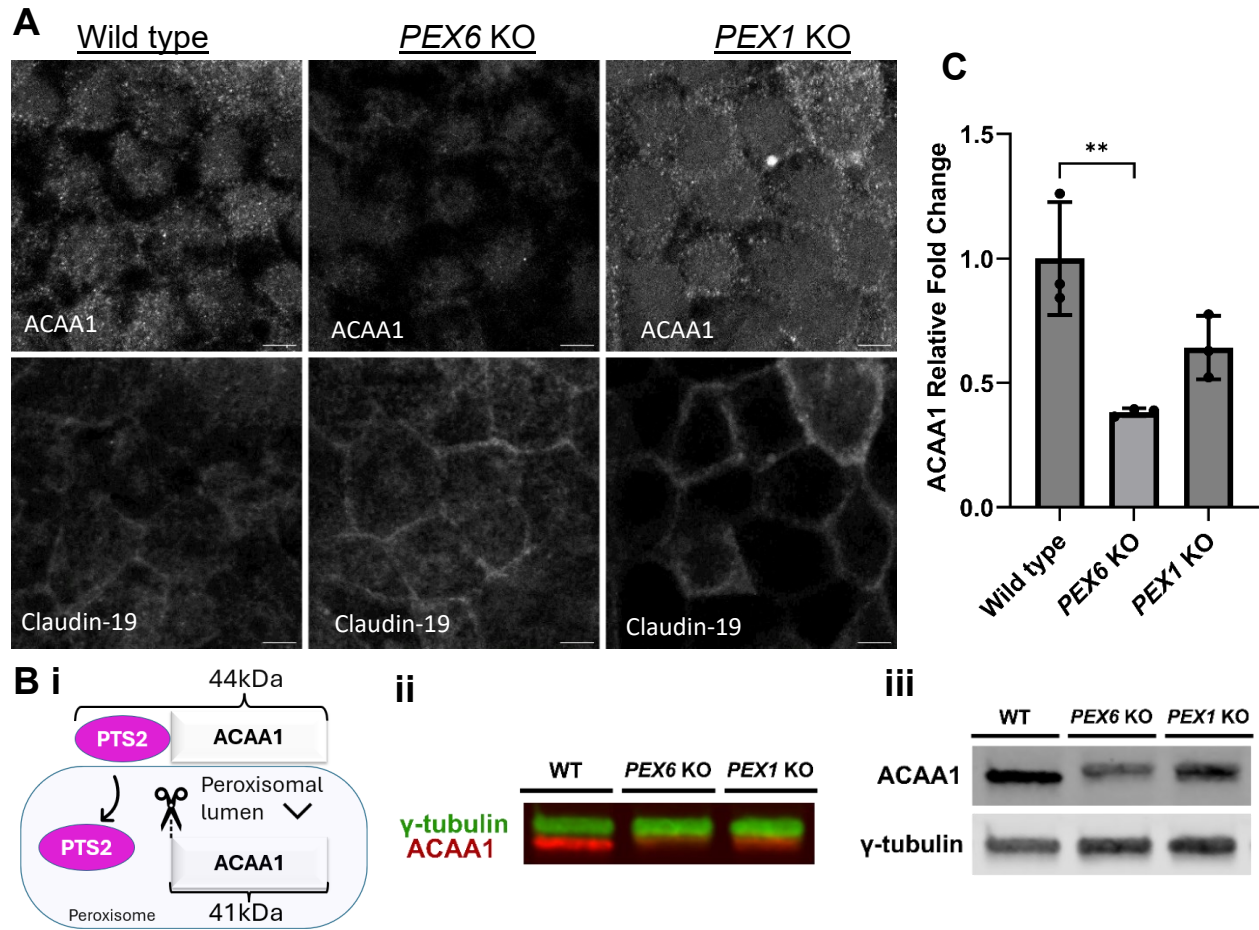


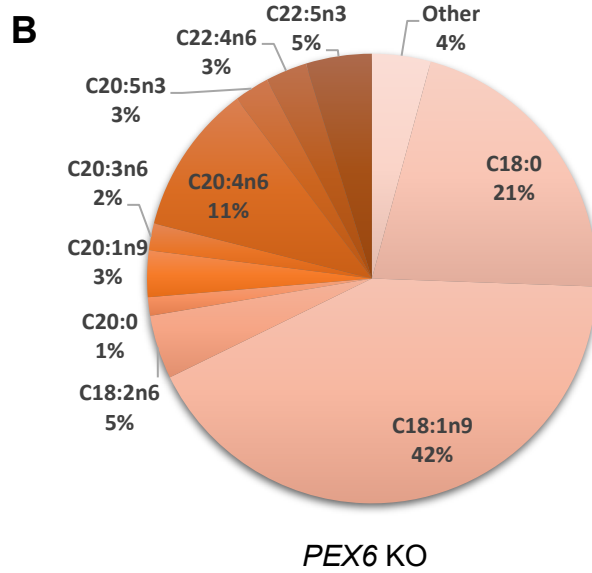
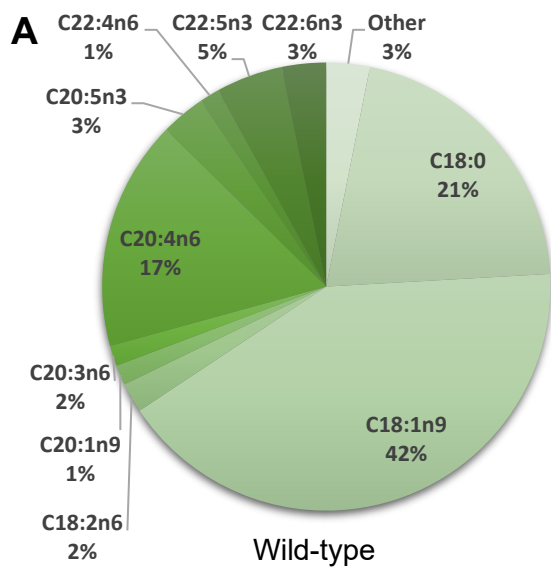
Figure 8. Evaluating peroxisome matrix protein import by assessing ACAA1 distribution and processing. A) Maximum projection z-stacks of iRPE acquired using Leica SP5 confocal microscope. The scale bar is 5 μ m. B) Western blot analysis of the processing of ACAA1 was performed by probing PTS2-ACAA1 (uncleaved) and ACAA1 (cleaved) using the same antibody. a: ACAA1 peroxisomal import schematic adopted from Benson et al., 2021. b presents the merged image of c, acquired using a Li-Cor Odyssey CLx. γ -tubulin serves as a ladder and a loading control. d: Quantification of total ACAA1 (cleaved and uncleaved forms) normalized to γ -tubulin. 30 μ g of protein was loaded per well (n=3 technical replicates). One-way ANOVA $P=0.007$. Tukey's test $P=0.0058$.

3.4 Lipid Profiles of the Retinal Pigment Epithelium (iRPE)

Given the established role of peroxisomes in lipid metabolism, particularly in the catabolism of VLCFAs and synthesis of DHA, the fatty acid profiles of peroxisome exportomer-deficient iRPE were analyzed relative to wild-type cells. Quantitative gas chromatography–flame ionization detection (GC-FID) was performed by Creative Proteomics, and only *PEX6* KO and wild-type iRPE were analyzed due to cost limitations. Of the C18–C26 fatty acids probed, arachidonic acid (C20:4n6) was the third-most abundant fatty acid with 17% prevalence in wild-type iRPE (Figure 9A) and 11% prevalence in *PEX6* KO iRPE (Figure 9B). C22:4n6, one β -oxidation event upstream of C20:4n6, was significantly elevated in the *PEX6* KO iRPE relative to wild-type iRPE ($P < 0.0001$) (Figure 9C).

In the *PEX6* KO iRPE, α -linolenic acid (C18:3n3) was significantly elevated, and DHA (C22:6n3) was significantly reduced relative to wild-type iRPE ($P < 0.0001$) (Figure 9C). DHA (C22:6n3) is synthesized in peroxisomes from the α -linolenic acid (C18:3n3) precursor (Figure 9D) (Swinkels & Baes, 2023).

In addition, C18:2n6, C18:3n6, C20:0, C20:1n9, C20:n6, and C24:0 were all significantly elevated in the *PEX6* KO iRPE relative to wild-type cells ($P < 0.0001$). C26:0 levels did not differ significantly between *PEX6* KO iRPE and wild-type cells ($P > 0.99$).



● Wild type
▲ PEX6 KO

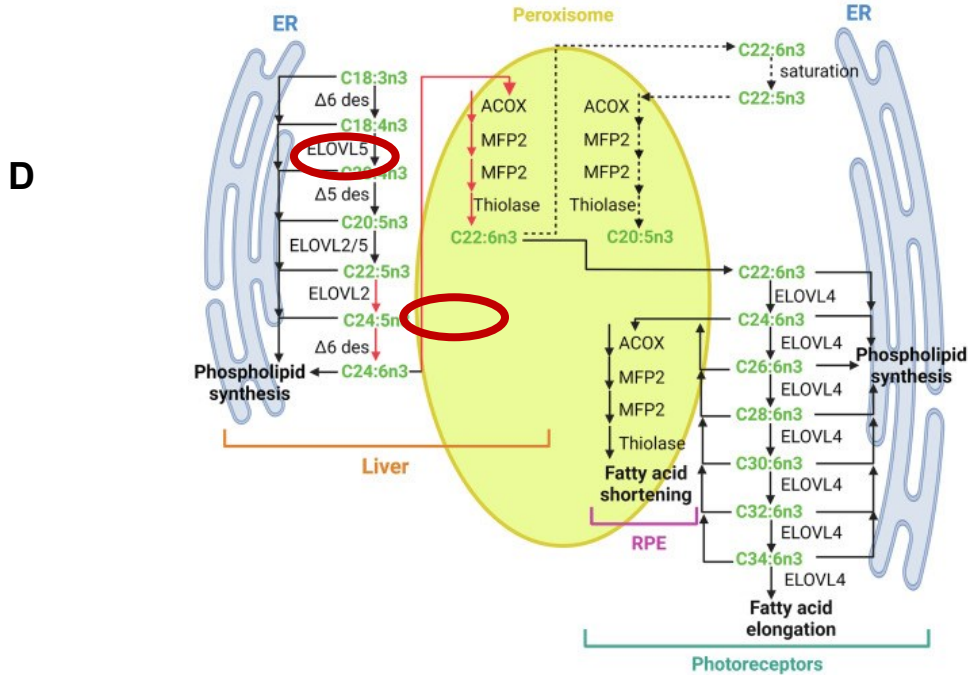
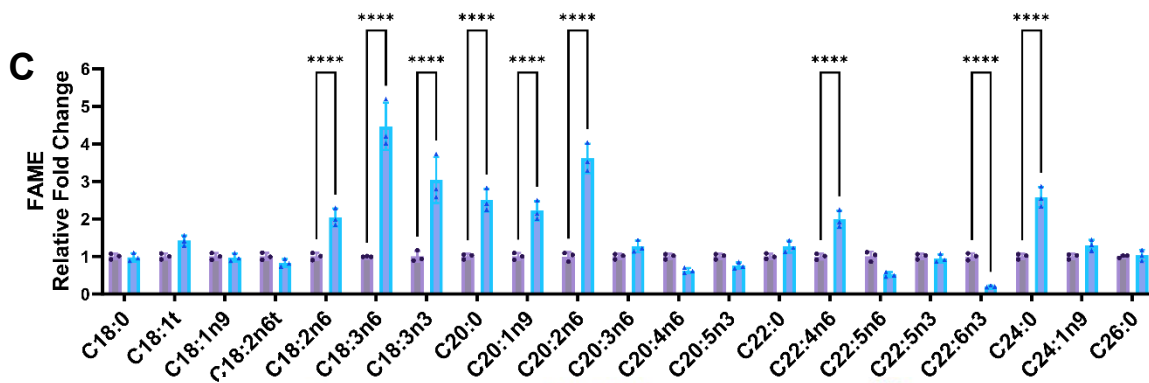


Figure 9. A comparison of the fatty acid profiles of PEX6 KO and wild-type iRPE. iRPE were subject to quantitative gas chromatography–flame ionization detection (GC-FID) (n=3 technical replicates). Fatty acids were identified and quantified by comparison to a standard mixture of fatty acids; detected fatty acid methyl ester (FAME) were presented (C). Two-way ANOVA $P < 0.0001$ for the genotype, fatty acids, and interaction. Sidak's test indicated by **** $P < 0.0001$. Pie charts present the relative abundance of detected fatty acids in wild-type iRPE (A) and PEX6 KO iRPE (B). D) A schematic highlighting DHA (C22:6n3) production in peroxisomes. Adapted from Swinkels & Baes, 2023.

3.5 Photoreceptor Outer Segment Challenge

3.5.1 Immunofluorescence

One of the main functions of the RPE is the phagocytosis of POS and subsequent metabolism of the lipid-rich contents. Immunofluorescence microscopy was used to test the hypothesis that peroxisome exportomer-deficient iRPE accumulate lipid relative to wild-type cells at baseline (unfed) and following POS addition (fed). BODIPY 493/503 staining and PLIN2 immunofluorescence demonstrated the presence of more LDs in unfed *PEX1* KO and *PEX6* KO iRPE relative to unfed wild-type iRPE (Figure 10). Following POS feeding, all iRPE accumulated LDs, as supported by increased BODIPY 493/503 and PLIN2 signals (Figure 10). Fed *PEX1* KO and *PEX6* KO iRPE had relatively more LDs than fed wild-type iRPE. Fed *PEX6* KO iRPE had larger LDs compared to fed *PEX1* KO and wild-type iRPE (Figure 10).

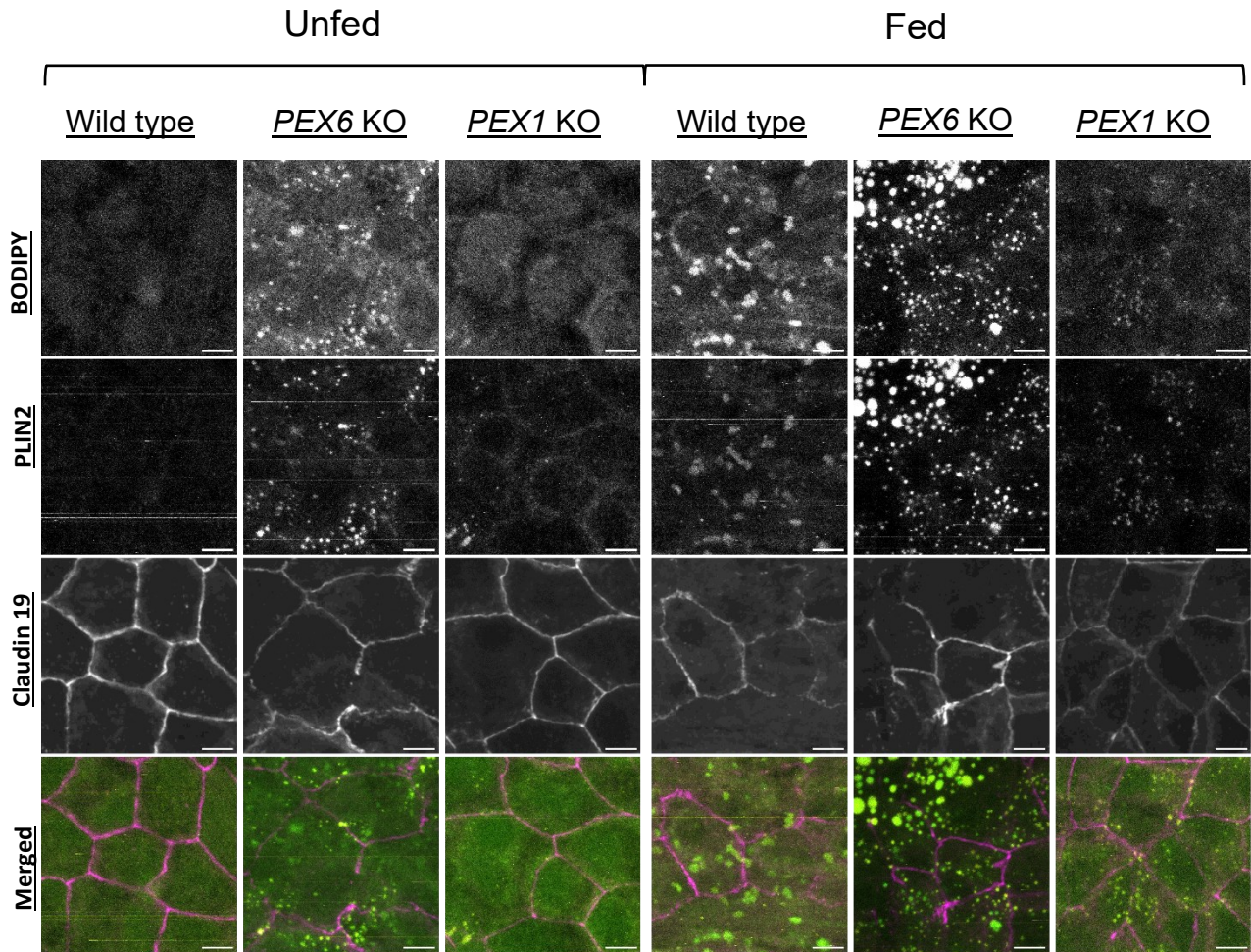


Figure 10. Immunofluorescence detection of lipid accumulation in iRPE following photoreceptor outer segment challenge. Maximum intensity projections of z-stacks captured using a Leica SP5 confocal microscope. iRPE were challenged with 10 POS/cell for 7 consecutive days. Unfed cells were subjected to daily media changes lacking POS. BODIPY 493/503 and anti-PLIN2 were applied to detect neutral lipid droplets. Claudin-19 highlights cell borders. The scale bar is 5 μ m.

3.5.2 Flow Cytometry

Flow cytometry was used to quantify intracellular neutral lipid accumulation in iRPE in both unfed and fed conditions. Following POS addition (fed), the relative BODIPY 493/503 MFI change to the baseline (unfed) of wild-type, *PEX6* KO, and *PEX1* KO was 0.49, 0.65, and 0.78 respectively. Relative to unfed wild-type iRPE, unfed *PEX6* KO iRPE had 3 times more BODIPY 493/503 MFI, and unfed *PEX1* KO iRPE had 2 times more BODIPY MFI (Figure 11A). Following POS feeding, both *PEX6* KO and *PEX1* KO iRPE had approximately double the BODIPY MFI relative to fed wild-type iRPE (Figure 11A). PLIN2 detection in fed compared to unfed iRPE showed an accumulation of LDs, confirmed by the ring localization of PLIN2 (Figure 11B). LDs were larger in fed *PEX6* KO and *PEX1* KO iRPE relative to fed wild-type iRPE (Figure 11B). LDs were detected at a single intracellular plane identified by tight junction labeling (Supplementary Figure 6).

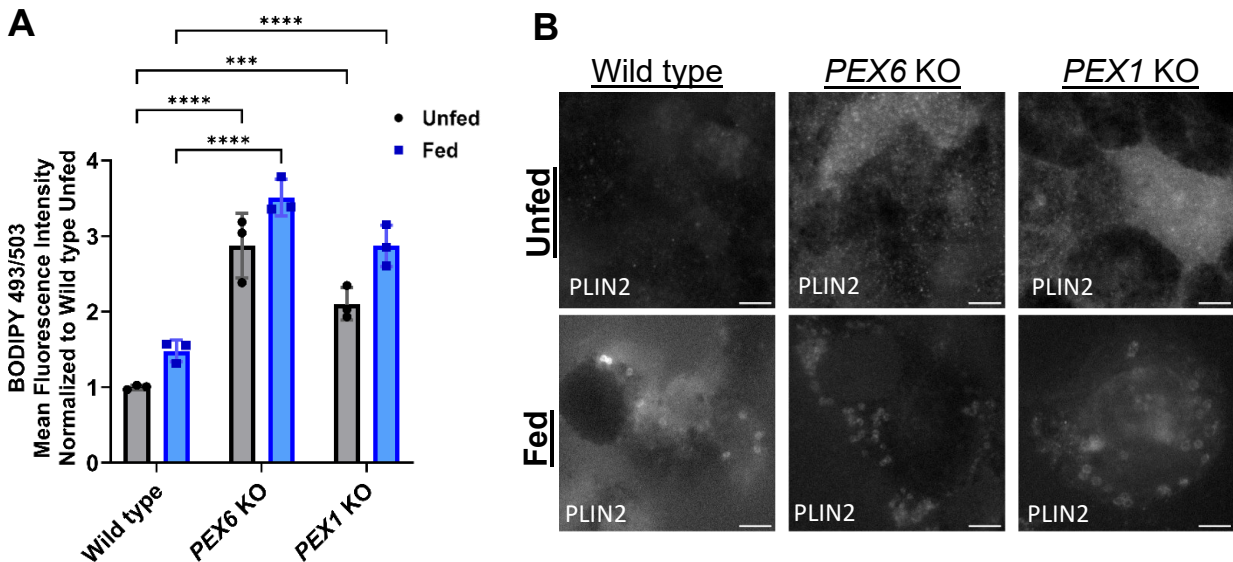


Figure 11. Flow cytometry-based quantification of lipid accumulation in iRPE following POS challenge. iRPE were challenged with 10 POS/cell for 7 consecutive days. Unfed cells were subjected to daily media changes lacking POS. BODIPY 493/503 and anti-PLIN2 were applied to detect neutral lipid accumulation. A) Intracellular neutral lipid quantification with BODIPY 493/503 using flow cytometry (n=3 technical replicates). Two-

way ANOVA testing for genotype-based differences in neutral lipid detection; $P < 0.0001$. Two-way ANOVA testing for POS feeding-induced differences in neutral lipid detection; $P = 0.0002$. Both unfed *PEX6* and *PEX1* KO iRPE and fed *PEX6* and *PEX1* KO iRPE had significantly higher BODIPY 493/503 MFI (Mean Fluorescence Intensity) compared to unfed and fed wild-type iRPE, respectively. Tukey's comparisons are indicated by *** $P = 0.0005$ and **** $P < 0.0001$. B) Single-plane microscopy images of unfed and fed iRPE cells labelled with PLIN2, captured using a Leica Thunder. Scale bar is 5 μ m.

4. Discussion

4.1 Effectiveness of a Human Stem-Cell Derived Model of Peroxisome Dysfunction in the Retinal Pigment Epithelium

PBDs are multisystem diseases that may manifest as hepatic dysfunction, neurodegeneration, and vision loss, among other pathologies (Baes & Van Veldhoven, 2016). The severity of the disease is dependent on the severity of peroxisomal dysfunction. In addition, the disease phenotype in each organ may be strongly associated with each organ's dependence on intact peroxisome function. Clinical and fundamental science findings strongly suggest that retinal degeneration in patients with PBDs is associated with RPE dysfunction and atrophy (Benson et al., 2021; Das et al., 2021). Therefore, the RPE is a highly relevant retinal cell type to study in the context of PBD-related retinal degeneration.

Here, I generated the first peroxisomal exportomer-deficient human iRPE. Of note, all three iRPE populations including wild-type, *PEX1* KO, and *PEX6* KO, share the same isogenic background which controls for confounding genetic variables. The mutant iRPE were generated from the same wild-type iPSCs, and included the introduction of a homozygous single base insertion that caused a premature stop codon in *PEX1* or *PEX6* transcripts (Figure 6). These early frameshift mutations are anticipated to cause nonsense-mediated mRNA decay as opposed to protein truncation. This was confirmed for the *PEX6* KO, where no *PEX6* protein was detected by western blotting using an anti-*PEX6* antibody that recognized the N-terminus (Figure 6). Whether the *PEX1* KO causes nonsense-mediated mRNA decay remains to be confirmed by RNA studies, since the anti-*PEX1* antibody recognized the C-terminus and would not be expected to bind truncated *PEX1*.

On one hand, the *PEX1* KO, *PEX6* KO, and wild-type iRPE all recapitulate native RPE features. The cells are pigmented and demonstrate basal fluid secretion as evident by bubbles forming under iRPE in culture (Figure 6) (Dvoriashyna et al., 2020). *PAX6*, a

marker of RPE progenitor cells, and MITF, a marker of committed RPE, were highly expressed in the differentiated iRPE. PAX6 was expressed at a higher level than anticipated in our cultures that otherwise expressed RPE markers and developed pigment and tight junctions consistent with fully differentiated and mature iRPE. Depending on the differentiation protocol, PAX6 expression varies (Wu et al., 2016); this intrinsic variability may account for the higher PAX6 expression levels in my iRPE. Therefore, examining multiple signature RPE markers to evaluate purity and differentiation quality is important. My iRPE populations are shy of clinical-grade iRPE, which generally requires >98% homogeneity, but make for excellent research-grade models as approximately 91% of all cells were positive for iRPE-signature proteins detected by flow cytometry (Table 2). iRPE monolayers displayed a cobblestone morphology and formed tight junctions as evident by immunolabeling of Claudin-19 and ZO-1 (Figure 6, Supplementary Figure 2). Additionally, the resulting iRPE successfully internalized POS added to the media.

On the other hand, I demonstrated that the peroxisomal exportomer complex is impaired in the *PEX1* KO and *PEX6* KO iRPE. Both PEX1 and PEX6 facilitate the ATP-dependent release of the monoubiquitinated receptor, PEX5, from the peroxisomal membrane to the cytosol for further rounds of matrix protein import (Law et al., 2017; Wanders et al., 2023). In the absence of PEX1 or PEX6, monoubiquitinated PEX5 accumulates at the peroxisomal surface and induces autophagosome-mediated degradation of peroxisomes (pexophagy) (Law et al., 2017). While both western blot and immunofluorescence experiments suggested reduced PMP70 abundance and a reduced number of PMP70-positive puncta in the mutant iRPE relative to wild-type, these did not reach statistical significance (Figure 7). Additional experimental replicates are required to determine if *PEX1* KO and *PEX6* KO iRPE indeed have fewer peroxisomes compared to wild-type cells.

ACAA1 is a peroxisomal matrix-destined enzyme that contains an N-terminus PTS2 signal of 9 amino acids. Once inside the peroxisomal lumen, the PTS2 nonapeptide is cleaved off ACAA1 by TYSND1, which is concentrated in the peroxisomal matrix. This processing of ACAA1 can be resolved by western blotting, and the same ACAA1 antibody detects both PTS2-ACAA1 (uncleaved) and ACAA1 (cleaved). When *PEX6* retains some

function, both PTS2-ACAA1 and ACAA1 bands are detected, implying that peroxisomal matrix protein import is partially intact (Benson et al., 2021). Western blot data convincingly demonstrates the detection of ACAA1 (cleaved from) in wild-type iRPE, implying intact matrix protein import, and PTS2-ACAA1 (uncleaved form) in both *PEX1* KO and *PEX6* KO iRPE, implying disrupted matrix protein import (Figure 8).

In summary, the generated *PEX1* KO and *PEX6* KO iRPE demonstrate native RPE features and exhibit peroxisomal matrix protein import deficiency, validating them as iRPE models of peroxisomal dysfunction.

The RPE is integral to sustaining retinal health and vision as it supports the neighbouring light-sensing photoreceptors. Kocherlakota et al. (2023) explored the role of peroxisomes in the RPE by knocking-out peroxisomal fatty acid beta-oxidation multifunctional protein 2 (*Mfp2*), a central enzyme for peroxisomal β -oxidation, in murine RPE only, relying on the specificity of a *BEST1*-Cre recombinase for the RPE. The authors investigated the murine RPE cellular phenotype by examining both histological sections of the entire retina and RPE flat mounts (Ortolan et al., 2022). The murine RPE were severely atrophic when *Mfp2* was knocked-out. However, when POS formation was genetically blocked, a normal RPE phenotype was restored. The authors hypothesized that this occurred because the peroxisomal β -oxidation-deficient RPE were no longer burdened with the processing of lipid-rich POS (Kocherlakota et al., 2023). These experiments determined that peroxisomal β -oxidation is essential for the normal handling of POS by the RPE (Kocherlakota et al., 2023).

Despite established methods to study retinal function in animals, evaluating cell-autonomous disease mechanisms are more challenging to undertake in these models, highlighting the utility of cell culture. RPE cell culture has been extensively used to model RPE pathology (Bharti et al., 2022). Freshly collected eye tissue from human donors or animals can be used to establish primary RPE cultures. Depending on the source of the cultured RPE, the cells recapitulate the morphology observed in RPE flat mounts to varying degrees. Moreover, the RPE explants retain functionality as demonstrated by their ability to phagocytose POS (Mazzoni et al., 2019). However, RPE cells are post-mitotic,

and as a result, primary RPE cultures cannot be propagated beyond a few passages, limiting the number of experiments that can be performed.

Human-derived RPE cells, such as the spontaneously immortalized ARPE-19 cell line, overcome the restrictive post-mitotic feature intrinsic to primary RPE cells. Under certain culture conditions, ARPE-19 cells behave like native RPE (Hazim et al., 2019). If cultured appropriately, ARPE-19 cells may be used as a model to study human RPE biology (Pfeffer & Fliesler, 2022). However, immortalized RPE cell lines such as ARPE-19 cells remain genetically unstable and often have chromosomal abnormalities. In some ways, ARPE-19 cells fail to recapitulate *in vivo* RPE physiology. For instance, Claudin-19 is not expressed in ARPE-19 (Luo et al., 2006). The use of iPSC-derived RPE (iRPE) offers a methodology to generate essentially infinite numbers of human RPE cells from stem cells, and these iRPE faithfully recapitulate *in situ* RPE morphology and function (Bharti et al., 2022). Like primary RPE cultures, however, once differentiated and matured, iRPE may be passaged only a few times. iRPE generation protocols also allow for the reprogramming of patient-derived iPSCs to RPE, creating disease-in-a-dish models. Some protocols yield clinical-grade iRPE that may be transplanted to preserve or restore vision (Sharma et al., 2019). TYRP1 and PMEL17, markers of mature RPE, were detected in > 99% of clinical grade iRPE populations, whereas another RPE marker, BEST1, was detected in > 70% of cells (Sharma et al., 2019). The populations of iRPE that I differentiated are comparable and exhibited high purity (Table 2). TYRP1 and PMEL17 were detected, on average, in 88% and 92% of my iRPE populations, respectively, whereas BEST1 was detected in 92% of my iRPE (Table 2).

Additionally, studying iRPE in isolation proved effective in demonstrating RPE-autonomous pathologies that were previously attributed to different cell types. Stargardt disease, caused by biallelic mutations in the *ABCA4* gene, was previously thought to only cause disease due to pathological changes in the POS content handled by the RPE (Farnoodian et al., 2022). Impaired *ABCA4* function in photoreceptors was thought to drive the disease mechanism by altering the POS load phagocytosed by the RPE which would contain indigestible material. Recently, *ABCA4* knockout iRPE exhibited

intracellular lipid handling defects that compound the disease pathology (Farnoodian et al., 2022). The *ABCA4* knockout iRPE did not effectively digest wild-type POS relative to wild-type iRPE, highlighting an iRPE autonomous phenotype in addition to the previously known disease-causing changes in photoreceptor cells.

4.2 Differentiation of *PEX1* and *PEX6* Knockout Retinal Pigment Epithelium

Mutations in *PEX1* and *PEX6* together account for approximately two-thirds of all PBDs (Tan et al., 2018). Complete loss-of-function mutations in *PEX1* or *PEX6* are lethal in multicellular organisms (Rinaldi et al., 2017).

RPE-specific impairment of an integral peroxisomal β -oxidation enzyme in mice resulted in de-differentiation of the RPE, demonstrated by loss of cell polarity (Kocherlakota et al., 2023). When *PEX1* or *PEX6* are absent, at least one peroxisomal β -oxidation enzyme fails to localize to the peroxisomal matrix as demonstrated by a cytosolic distribution of ACAA1 (Figure 8A) and the exclusive detection of PTS2-ACAA1 (uncleaved form), implying disrupted matrix protein import, in the *PEX1* KO and *PEX6* KO iRPE (Figure 8B). Likely, these peroxisomes can no longer compartmentalize β -oxidation, despite the potential presence of VLCFAs in the peroxisomal lumen because of their intact ABCD peroxisomal membrane transporters. *PEX1* KO and *PEX6* KO iRPE likely suffer from dysfunctional peroxisomal β -oxidation because ACAA1, and potentially other enzymes, fail to reach the peroxisomal lumen. Differentiation of all 3 cell lines took place simultaneously. From observation under a light microscope, the wild-type, *PEX1* KO, and *PEX6* KO cells all progressed and differentiated similarly from the iPSC stage until the fully-mature iRPE stage. This seems to be in contrast to the RPE de-differentiation phenotype reported in *Mfp2* knockout mice (Kocherlakota et al., 2023), but a more detailed analysis of cell morphometry in all 3 iRPE lines is planned for the future. The successful differentiation of the *PEX1* KO and *PEX6* KO iRPE lines suggests that intact peroxisome function may not be essential for the development and maturation of RPE cells in culture.

Ott and colleagues also demonstrated a peroxisomal matrix protein import defect in *PEX1* KO T-REx™-293 cells, immortalized human embryonic kidney cells (Ott et al., 2023). After inspecting 16 cells, the authors concluded that there were more PMP70-positive puncta in *PEX1* KO T-REx™-293 compared to control cells. On the contrary, I found that my *PEX1* KO iRPE had fewer PMP70-positive puncta compared to wild-type iRPE, although this did not reach statistical significance (Figure 7). Both experiments employed the same software to detect PMP70-positive spots. However, the number of spots was not normalized to the respective cell volume in the *PEX1* KO T-REx™-293 cells, which may explain the discrepancy. PMP70 is inserted into the peroxisome membrane by PEX19, independent of the PEX1 and PEX6 function (Jones et al., 2004).

4.3 Lipid Profiles in Retinal Pigment Epithelium with Abnormal Peroxisome Function

Peroxisomes compartmentalize metabolic reactions such as the oxidation of fatty acids and synthesis of ether lipids to regulate intracellular lipid homeostasis. When the peroxisomal molecular machinery is hindered, or peroxisomal enzymes are deficient, the reactions housed inside peroxisomes are impaired. In PBDs, peroxisomal matrix enzymes may fail to reach the peroxisomal lumen, which was the case for the *PEX1* KO and *PEX6* KO iRPE. Lack of the peroxisomal enzymatic capacity is indirectly caused by the absence of PEX1 or PEX6 because peroxisomal matrix proteins cannot be effectively imported into peroxisomes. The loss of PEX1 or PEX6 that contribute to the peroxisomal exportomer complex prevents the recycling of PEX5, a receptor that shuttles peroxisomal matrix-destined enzymes, including those that participate in lipid metabolism. *PEX6* KO iRPE exhibited an altered intracellular lipid profile relative to wild-type iRPE (Figure 9C).

Clinically, fatty acid changes in patient plasma support the biochemical diagnosis of peroxisomal disorders. Patients with PBDs frequently present with elevated plasma levels of VLCFAs (C26:0, C24:0, C26:0/C22:0, and C24:0/C22:0) and the branched-chain fatty acids phytanic acid and pristanic acid (De Biase et al., 2020; Herzog et al., 2018). Similarly, when the central β -oxidation enzyme, *Mfp2*, is knocked-out in mice, VLCFAs and

branched-chain fatty acids are elevated in murine plasma (Baes et al., 2000). Additionally, when the β -oxidation enzyme, Mfp2, is absent in the RPE only, cellular lipid changes were detected in the RPE. Notably, C26:0 was elevated and C22:6n3 was reduced in mutant murine RPE relative to wild-type (Kocherlakota et al., 2023). To produce DHA (C22:6n3), elongase and desaturase enzymes act on C18:3n3 to generate C24:6n3, which is then subject to β -oxidation inside peroxisomes to yield C22:6n3 (Figure 9D) (Swinkels & Baes, 2023). When peroxisomes are no longer housing enzymatic reactions normally, there are reduced levels of DHA and a corresponding accumulation of DHA precursors because the final β -oxidation step does not occur. The lipid profile of *PEX6* KO iRPE showed significantly elevated levels of C24:0, C18:3n3 (a DHA precursor), and reduced DHA (C22:6n3) relative to wild-type iRPE. However, levels of C26:0 were unexpectedly similar between *PEX6* KO iRPE and wild-type iRPE (Figure 9C). The C26:0 corresponds to less than 0.5% of the total fatty acids detected in the GC-FID experiment. Future experiments adding C26:0 to the cells in the media or via POS could uncover a significant processing difference between *PEX6* KO and wild-type iRPE. The increased C24:0 that I identified in *PEX6* KO iRPE is in line with the clinical presentation of a patient with complete loss-of-function of *PEX6* as elevated serum VLCFAs levels are expected. The lack of DHA in the *PEX6* KO iRPE strongly highlights the requirement of healthy peroxisomes for DHA synthesis. As a result of the defective peroxisome exportomer complex, DHA is not produced because peroxisomes are expected to be lacking the necessary enzyme for its final β -oxidation reaction. Instead, presumed metabolic backlog causes a significant increase in the DHA precursor, C18:3n3 (Figure 9C). In addition to its intracellular synthesis, a large amount of DHA is obtained from our diet and delivered to the retina through the activity of basal major facilitator superfamily domain-containing protein 2a channels (MFSD2A) (Lewandowski et al., 2022). GC-FID data highlight the ability of RPE cells in culture to synthesize DHA, and demonstrate the requirement for intact peroxisomes for this process (Figure 9C).

In vivo, lipid-rich POS must be metabolized and recycled by the RPE, exposing the cells to relatively large amounts of VLCFAs. Peroxisomes in the RPE are required to support the

degradation of VLCFAs from ingested POS. To simulate native physiology, isolated bovine POS were added to iRPE in the culture media. Degraded POS lipids have been shown to be transiently stored in RPE lipid droplets (LDs) (Chen & Anderson, 1993). Therefore, I examined LDs in iRPE to assess lipid accumulation following POS feeding. BODIPY 493/503 staining demonstrated the striking increase in the size and number of LDs following POS feeding in *PEX6* KO and *PEX1* KO iRPE relative to wild-type iRPE (Figure 10). Flow cytometry was used to quantify the BODIPY 493/503 mean signal intensity of iRPE that were cultured on transwells and subjected to the same POS challenge. *PEX6* KO and *PEX1* KO iRPE had significantly more neutral lipid accumulation at baseline and post-POS feeding compared to wild-type iRPE (Figure 11). PLIN2 immunofluorescence was performed to validate the detection of LDs by BODIPY 493/503, since PLIN2 is an exclusive LD marker (Heid et al., 1998; McIntosh et al., 2012) (Figures 7 and 8).

At baseline, in the absence of POS, *PEX6* KO and *PEX1* KO iRPE showed significant neutral lipid accumulation (Figure 11A). In fasting-induced lipolysis, PEX5 delivers adipose triglyceride lipase (ATGL) to LDs (Kong et al., 2020). Cytosolic PEX5 is hypothesized to be reduced in the peroxisome exportomer-deficient iRPE, which may have contributed to the accumulation of LDs due to reduced PEX5-mediated shuttling of ATGL to LDs. Future studies could evaluate the distribution of ATGL in peroxisome exportomer-deficient iRPE compared to wild-type cells under starvation conditions. One of the E3 ubiquitin ligases, PEX2, is also known to modulate ATGL activity via ubiquitination (Ding et al., 2021); however, PEX2 function was not explored in the iRPE. Additionally, fluorescently labelled fatty acid conjugates targeted to the peroxisomal lumen via PMP70 result in increased fluorescence in peroxisomes when peroxisome-ER vesicle-associated membrane protein-associated protein (VAP) contact sites are disrupted, suggesting that peroxisomal fatty acid retention is influenced by ER interactions (Hua et al., 2017; Korotkova et al., 2024). Disrupted interactions between peroxisomes, LDs, and the ER in *PEX1* KO and *PEX6* KO iRPE may underly the intracellular accumulation of LDs (Figure 11). The precise mechanism of intracellular lipid accumulation in my *PEX1* and *PEX6* KO iRPE models warrants further investigation.

Following POS feeding, *PEX1* KO and *PEX6* KO iRPE showed significantly higher intracellular neutral lipid accumulation compared to wild-type iRPE (Figure 11A). Peroxisomes may handle POS-derived lipids directly from interactions with lysosomes (Chu et al., 2015). Alternatively, peroxisomes may handle the POS-derived lipids by interacting with LDs since the phagocytosed POS lipid content is transiently stored in LDs (Chen & Anderson, 1993). In addition to any potentially disrupted organellar interactions, *PEX1* KO and *PEX6* KO iRPE have defective peroxisomal matrix protein import and would be anticipated to fail to metabolize POS-derived fatty acids via β -oxidation.

Ultimately, the enzymatic reactions normally housed inside peroxisomes substantially influence lipid profiles in iRPE, as evident in my GC-FID and flow cytometry assays. These experiments demonstrated both a significant accumulation of neutral lipids and differences in the abundance of various fatty acids when the peroxisomal exportomer complex is impaired (Figure 9 and 11). Interestingly, an accumulation of LDs has been shown to reduce the function of ARPE-19 cells in culture. When LDs were induced by supplementing the media with oleic acid (C18:1), ARPE-19 cells ingested fewer POS (Yako et al., 2022). A reduced capacity to effectively phagocytose POS *in vivo* negatively affects photoreceptor function and leads to vision loss (Ramsden et al., 2017). Lipid accumulation can be indirectly detected in the RPE of patients by capturing fundus autofluorescence images in the clinic. These images recognize lipofuscin, which is a complex of protein and lipids that build up in diseased RPE (Kennedy et al., 1995). Patients with PBDs frequently have hyperautofluorescence evident on imaging, implying lipofuscin accumulation and RPE stress. Thus, human-derived iRPE models can be used to correlate lipid metabolism in iRPE in culture with clinical findings in patients with PBDs. In addition, these iRPE models that recapitulate retinopathy in PBD patients can enhance our understanding of the role of peroxisomes in lipid metabolism in the RPE. This insight may shed light on disease mechanisms and potential therapeutic approaches for other disorders involving dysregulated lipid metabolism in the RPE, such as age-related macular degeneration.

4.4 Study Limitations

One of the intrinsic limitations of my project was that the roles of PEX1 and PEX6 were evaluated in RPE grown in cell culture. While studying cells in isolation informs cell-autonomous phenotypes, the cells exist in a complex tissue system in organisms. The RPE facilitates the transport of nutrients from the basal choroidal circulation to the apical neural retina. Environmental stimuli can contribute to the physiology of the RPE. For example, the ingestion of POS by the RPE follows the circadian cycle. In cell culture, POS were added at the same time each day to help mimic this natural cycle; however, the more complex interactions that occur between RPE and entire photoreceptors cannot be easily studied in cell culture. In the context of studying peroxisomal dysfunction in the RPE, a mouse model was recently well-characterized (Kocherlakota et al., 2023). Since PBDs are largely syndromic disorders with dysfunction occurring in multiple body systems, animal models are critical for studying how disease in one tissue, such as the liver, may affect another tissue, such as the retina, in patients with PBDs. The iRPE models of peroxisome dysfunction that I have developed complement recent studies in mice. Both animal and cell culture models are needed to understand disease processes and develop vision-saving therapies for patients.

A second limitation that arises when working with iRPE is that obtaining biological experimental replicates is not always feasible. Since iRPE cultures are laborious and costly to generate, differentiating independent populations of iPSCs from the same cell line at different times is cost- and time-prohibitive. Therefore, each iRPE cell line was differentiated from iPSCs one time only. For downstream assays, the same original population of mature iRPE for each line was plated, so any experimental replicates using iRPE are truly technical replicates. Given the substantial cost and time investment for iPSC-RPE differentiation, using technical replicates for experiments in iRPE is an accepted practice (Farnoodian et al., 2023; Nguyen et al., 2015).

A third limitation of the study was that the observed trend of fewer PMP70-positive puncta in *PEX1* KO and *PEX6* KO iRPE failed to reach statistical significance ($P=0.29$).

because a stringent statistical approach was applied with an insufficient sample size. As a result, my hypothesis that *PEX1* KO and *PEX6* KO iRPE have fewer peroxisomes (presumably due to increased pexophagy) compared to wild-type iRPE cannot be conclusively addressed. Additional independent cell culture replicates are required to determine whether a true difference in the number of PMP70-positive puncta exists between *PEX1* KO, *PEX6* KO, and wild-type iRPE.

Finally, despite using a published protocol to isolate bovine POS, the size, morphology, and lipid composition of the generated POS varies greatly. This discrepancy could affect the measured intracellular neutral lipid content in baseline (unfed) and POS-challenged (fed) iRPE among the cell lines. The variability in the isolated POS is difficult to control, since accurately identifying individual POS fragments is challenging. Other laboratories that work with RPE cultures acquire their POS from a single commercial source (InVision BioResources), thus reducing some of this inherent variability and maintaining a degree of inter-lab consistency. My lab has recently obtained POS from the same commercial source, and we plan on experimentally comparing these POS to those we isolated ourselves.

4.5 Future Directions

4.5.1 Generating Patient-Derived Retinal Pigment Epithelium

Fibroblasts from a patient with a *PEX6*-related PBD have been successfully reprogrammed to iPSCs in my lab. Although this patient has substantial retinal degeneration and vision impairment, his overall systemic disease burden is relatively mild considering the entire spectrum of severity of PBDs. This is reflected by a partial loss-of-function of *PEX6* (Benson et al., 2021). Differentiating these patient-derived iPSCs to iRPE will enable study of how a genetically milder type of PBD can still cause substantial retinopathy. In addition, we can compare this *PEX6* partial loss-of-function iRPE model to the *PEX6* KO iRPE to better understand the specific requirement for *PEX6* in the RPE.

4.5.2 DHA Supplementation

DHA is a product of intact peroxisomes with normal β -oxidation. In peroxisome-related disease states, systemic DHA levels are reduced (Klouwer et al., 2015). Up to 50% of the lipid content of POS is comprised of DHA, and the RPE is involved in the recycling of DHA following the phagocytosis of POS (Bazan, 2006; Rotstein et al., 2003). There is evidence that DHA may also protect the RPE from oxidative stress (Marcheselli et al., 2010). When peroxisomal β -oxidation is impaired, DHA supplementation was found to improve the ability of the RPE to process and metabolize POS in the short term (Swinkels et al., 2023). Additionally, DHA has been proposed to regulate lipid signalling pathways and inhibit lipogenesis (Han et al., 2023; Landowski et al., 2020, 2023). *PEX6* KO iRPE generate minimal DHA (Figure 9). These iRPE exhibited an increase in the size and number of LDs (Figure 10) and an accumulation of intracellular neutral lipids (Figure 11) relative to wild-type iRPE. I hypothesize that supplementing these cells with exogenous DHA will bolster the lipid homeostasis in the iRPE and will reduce intracellular lipid accumulation because DHA is expected to inhibit lipogenesis (Han et al., 2023). This experiment is currently underway in the lab.

4.5.3 Mimicking Photoreceptor Outer Segment Lipids Using Synthetic Liposomes

POS particles are widely used in cell culture models to study the critical role of the RPE in the phagocytosis of POS in normal and diseased states. However, isolating POS from animals introduces a degree of bias in downstream assays as the quality of the POS preparation, including the size, morphology, and biomolecule composition varies considerably and is difficult to control. Since the lipid composition of POS has been well-characterized, generating synthetic liposomes that mimic the lipid composition of POS will be attempted (Akbarzadeh et al., 2013; Anderson & Maude, 1970; Aveldaño & Bazán, 1983; Goldberg et al., 2016; Stone et al., 1979). I hypothesize that the iRPE will phagocytose and metabolize these liposomes similar to how the RPE processes POS. This will be confirmed using fluorescently-labelled phospholipid species to facilitate the

visualization of liposome uptake by the iRPE. This novel approach enables the manipulation of the individual lipid components within the liposomes to uncover RPE lipid metabolism pathways that could not be easily dissected with animal-derived POS. We plan on generating two distinct liposome populations: one that contains predominantly short-chain and medium-chain fatty acids, and another that contains predominantly long-chain and very long-chain fatty acids. Considering that mammalian peroxisomes exclusively oxidize very long-chain fatty acids prior to their further oxidation by mitochondria, this approach will help determine which fatty acids contribute most to LDs accumulation in iRPE with normal and impaired peroxisome function.

4.6 Concluding Remarks

Peroxisome biogenesis disorders (PBDs) frequently cause RPE dysfunction, retinal degeneration, and blindness. There is an urgent need to elucidate disease mechanisms so that therapeutic targets may be identified and vision-restoring treatments developed for patients. To study the cell-autonomous effect of peroxisome dysfunction in the RPE, *PEX1* KO, *PEX6* KO, and wild-type iRPE were successfully differentiated, validated, and characterized. *PEX1* KO and *PEX6* KO iRPE had deficient peroxisome matrix protein import and both iRPE accumulated lipids under basal and POS-challenged conditions relative to wild-type cells. My work has established the first models of peroxisome exportome deficiency in iRPE and demonstrated that these iRPE have altered lipid metabolism. These models can be used to further understand mechanisms of disease in PBDs, to explore the consequences of disrupted lipid metabolism on RPE function, and, more broadly, to study the role of peroxisomes in the RPE.

References

- Adijanto, J., Du, J., Moffat, C., Seifert, E. L., Hurley, J. B., & Philp, N. J. (2014). The Retinal Pigment Epithelium Utilizes Fatty Acids for Ketogenesis. *Journal of Biological Chemistry*, 289(30), 20570–20582. <https://doi.org/10.1074/jbc.M114.565457>
- Akbarzadeh, A., Rezaei-Sadabady, R., Davaran, S., Joo, S. W., Zarghami, N., Hanifehpour, Y., Samiei, M., Kouhi, M., & Nejati-Koshki, K. (2013). Liposome: Classification, preparation, and applications. *Nanoscale Research Letters*, 8(1), 102. <https://doi.org/10.1186/1556-276X-8-102>
- Ali, H., Kobayashi, M., Morito, K., Hasi, R. Y., Aihara, M., Hayashi, J., Kawakami, R., Tsuchiya, K., Sango, K., & Tanaka, T. (2023). Peroxisomes attenuate cytotoxicity of very long-chain fatty acids. *Biochimica et Biophysica Acta (BBA) - Molecular and Cell Biology of Lipids*, 1868(2), 159259. <https://doi.org/10.1016/j.bbalip.2022.159259>
- Anderson, R. E., & Maude, M. B. (1970). Lipids of ocular tissues. 6. Phospholipids of bovine rod outer segments. *Biochemistry*, 9(18), 3624–3628. <https://doi.org/10.1021/bi00820a019>
- Argyriou, C., D'Agostino, M. D., & Braverman, N. (2016). Peroxisome biogenesis disorders. *Translational Science of Rare Diseases*, 1(2), 111–144. <https://doi.org/10.3233/TRD-160003>
- Aveldaño, M. I., & Bazán, N. G. (1983). Molecular species of phosphatidylcholine, -ethanolamine, -serine, and -inositol in microsomal and photoreceptor membranes of bovine retina. *Journal of Lipid Research*, 24(5), 620–627.
- Baarine, M., Andréoletti, P., Athias, A., Nury, T., Zarrouk, A., Ragot, K., Vejux, A., Riedinger, J.-M., Kattan, Z., Bessede, G., Trompier, D., Savary, S., Cherkaoui-Malki, M., & Lizard, G. (2012). Evidence of oxidative stress in very long chain fatty acid – Treated oligodendrocytes and potentialization of ROS production using RNA interference-directed knockdown of ABCD1 and ACOX1 peroxisomal proteins. *Neuroscience*, 213, 1–18. <https://doi.org/10.1016/j.neuroscience.2012.03.058>

- Baes, M., Huyghe, S., Carmeliet, P., Declercq, P. E., Collen, D., Mannaerts, G. P., & Van Veldhoven, P. P. (2000). Inactivation of the Peroxisomal Multifunctional Protein-2 in Mice Impedes the Degradation of Not Only 2-Methyl-branched Fatty Acids and Bile Acid Intermediates but Also of Very Long Chain Fatty Acids. *Journal of Biological Chemistry*, 275(21), 16329–16336.
<https://doi.org/10.1074/jbc.M001994200>
- Baes, M., & Van Veldhoven, P. P. (2016). Hepatic dysfunction in peroxisomal disorders. *Biochimica et Biophysica Acta (BBA) - Molecular Cell Research*, 1863(5), 956–970.
<https://doi.org/10.1016/j.bbamcr.2015.09.035>
- Barillari, M. R., Karali, M., Di Iorio, V., Contaldo, M., Piccolo, V., Esposito, M., Costa, G., Argenziano, G., Serpico, R., Carotenuto, M., Cappuccio, G., Banfi, S., Melillo, P., & Simonelli, F. (2020). Mild form of Zellweger Spectrum Disorders (ZSD) due to variants in PEX1: Detailed clinical investigation in a 9-years-old female. *Molecular Genetics and Metabolism Reports*, 24, 100615.
<https://doi.org/10.1016/j.ymgmr.2020.100615>
- Barros-Barbosa, A., Ferreira, M. J., Rodrigues, T. A., Pedrosa, A. G., Grou, C. P., Pinto, M. P., Fransen, M., Francisco, T., & Azevedo, J. E. (2019). Membrane topologies of PEX 13 and PEX 14 provide new insights on the mechanism of protein import into peroxisomes. *The FEBS Journal*, 286(1), 205–222.
<https://doi.org/10.1111/febs.14697>
- Bazan, N. G. (2006). Cell survival matters: Docosahexaenoic acid signaling, neuroprotection and photoreceptors. *Trends in Neurosciences*, 29(5), 263–271.
<https://doi.org/10.1016/j.tins.2006.03.005>
- Benson, M. D., Papp, K. M., Casey, G. A., Radziwon, A., St Laurent, C. D., Doucette, L. P., & MacDonald, I. M. (2021). PEX6 Mutations in Peroxisomal Biogenesis Disorders. *Ophthalmology Science*, 1(2), 100028.
<https://doi.org/10.1016/j.xops.2021.100028>
- Bharti, K., Den Hollander, A. I., Lakkaraju, A., Sinha, D., Williams, D. S., Finnemann, S. C., Bowes-Rickman, C., Malek, G., & D'Amore, P. A. (2022). Cell culture models to study retinal pigment epithelium-related pathogenesis in age-related macular

- degeneration. *Experimental Eye Research*, 222, 109170.
<https://doi.org/10.1016/j.exer.2022.109170>
- Blenkinsop, T. A., Saini, J. S., Maminishkis, A., Bharti, K., Wan, Q., Banzon, T., Lotfi, M., Davis, J., Singh, D., Rizzolo, L. J., Miller, S., Temple, S., & Stern, J. H. (2015). Human Adult Retinal Pigment Epithelial Stem Cell–Derived RPE Monolayers Exhibit Key Physiological Characteristics of Native Tissue. *Investigative Ophthalmology & Visual Science*, 56(12), 7085. <https://doi.org/10.1167/iovs.14-16246>
- Borén, J., Taskinen, M. -R., Olofsson, S. -O., & Levin, M. (2013). Ectopic lipid storage and insulin resistance: A harmful relationship. *Journal of Internal Medicine*, 274(1), 25–40. <https://doi.org/10.1111/joim.12071>
- Bullock, J., Polato, F., Abu-Asab, M., Bernardo-Colón, A., Aflaki, E., Agbaga, M.-P., & Becerra, S. P. (2021). Degradation of Photoreceptor Outer Segments by the Retinal Pigment Epithelium Requires Pigment Epithelium-Derived Factor Receptor (PEDF-R). *Investigative Ophthalmology & Visual Science*, 62(2), 30.
<https://doi.org/10.1167/iovs.62.2.30>
- Caceres, P. S., & Rodriguez-Boulan, E. (2020). Retinal pigment epithelium polarity in health and blinding diseases. *Current Opinion in Cell Biology*, 62, 37–45.
<https://doi.org/10.1016/j.ceb.2019.08.001>
- Capowski, E. E., Simonett, J. M., Clark, E. M., Wright, L. S., Howden, S. E., Wallace, K. A., Petelinsek, A. M., Pinilla, I., Phillips, M. J., Meyer, J. S., Schneider, B. L., Thomson, J. A., & Gamm, D. M. (2014). Loss of MITF expression during human embryonic stem cell differentiation disrupts retinal pigment epithelium development and optic vesicle cell proliferation. *Human Molecular Genetics*, 23(23), 6332–6344.
<https://doi.org/10.1093/hmg/ddu351>
- Chang, C.-L., Weigel, A. V., Ioannou, M. S., Pasolli, H. A., Xu, C. S., Peale, D. R., Shtengel, G., Freeman, M., Hess, H. F., Blackstone, C., & Lippincott-Schwartz, J. (2019). Spastin tethers lipid droplets to peroxisomes and directs fatty acid trafficking through ESCRT-III. *Journal of Cell Biology*, 218(8), 2583–2599.
<https://doi.org/10.1083/jcb.201902061>

- Chen, H., & Anderson, R. E. (1993). Metabolism in Frog Retinal Pigment Epithelium of Docosahexaenoic and Arachidonic Acids Derived from Rod Outer Segment Membranes. *Experimental Eye Research*, 57(3), 369–377.
<https://doi.org/10.1006/exer.1993.1136>
- Chu, B.-B., Liao, Y.-C., Qi, W., Xie, C., Du, X., Wang, J., Yang, H., Miao, H.-H., Li, B.-L., & Song, B.-L. (2015). Cholesterol Transport through Lysosome-Peroxisome Membrane Contacts. *Cell*, 161(2), 291–306.
<https://doi.org/10.1016/j.cell.2015.02.019>
- Daniele, L. L., Caughey, J., Volland, S., Sharp, R. C., Dhingra, A., Williams, D. S., Philp, N. J., & Boesze-Battaglia, K. (2019). Peroxisome turnover and diurnal modulation of antioxidant activity in retinal pigment epithelia utilizes microtubule-associated protein 1 light chain 3B (LC3B). *American Journal of Physiology-Cell Physiology*, 317(6). <https://doi.org/10.1152/ajpcell.00185.2019>
- Das, Y., Swinkels, D., Kocherlakota, S., Vinckier, S., Vaz, F. M., Wever, E., Van Kampen, A. H. C., Jun, B., Do, K. V., Moons, L., Bazan, N. G., Van Veldhoven, P. P., & Baes, M. (2021). Peroxisomal Multifunctional Protein 2 Deficiency Perturbs Lipid Homeostasis in the Retina and Causes Visual Dysfunction in Mice. *Frontiers in Cell and Developmental Biology*, 9, 632930.
<https://doi.org/10.3389/fcell.2021.632930>
- De Biase, I., Tortorelli, S., Kratz, L., J. Steinberg, S., Cusmano-Ozog, K., & Braverman, N. (2020). Laboratory diagnosis of disorders of peroxisomal biogenesis and function: A technical standard of the American College of Medical Genetics and Genomics (ACMG). *Genetics in Medicine*, 22(4), 686–697.
<https://doi.org/10.1038/s41436-019-0713-9>
- Ding, L., Sun, W., Balaz, M., He, A., Klug, M., Wieland, S., Caiazzo, R., Raverdy, V., Pattou, F., Lefebvre, P., Lodhi, I. J., Staels, B., Heim, M., & Wolfrum, C. (2021a). Peroxisomal β -oxidation acts as a sensor for intracellular fatty acids and regulates lipolysis. *Nature Metabolism*, 3(12), 1648–1661. <https://doi.org/10.1038/s42255-021-00489-2>

- Ding, L., Sun, W., Balaz, M., He, A., Klug, M., Wieland, S., Caiazzo, R., Raverdy, V., Pattou, F., Lefebvre, P., Lodhi, I. J., Staels, B., Heim, M., & Wolfrum, C. (2021b). Peroxisomal β -oxidation acts as a sensor for intracellular fatty acids and regulates lipolysis. *Nature Metabolism*, 3(12), 1648–1661. <https://doi.org/10.1038/s42255-021-00489-2>
- Distel, B., Erdmann, R., Gould, S. J., Blobel, G., Crane, D. I., Cregg, J. M., Dodt, G., Fujiki, Y., Goodman, J. M., Just, W. W., Kiel, J. A., Kunau, W. H., Lazarow, P. B., Mannaerts, G. P., Moser, H. W., Osumi, T., Rachubinski, R. A., Roscher, A., Subramani, S., ... Veenhuis, M. (1996). A unified nomenclature for peroxisome biogenesis factors. *The Journal of Cell Biology*, 135(1), 1–3. <https://doi.org/10.1083/jcb.135.1.1>
- Dvoriashyna, M., Foss, A. J. E., Gaffney, E. A., & Repetto, R. (2020). Fluid and solute transport across the retinal pigment epithelium: A theoretical model. *Journal of The Royal Society Interface*, 17(163), 20190735. <https://doi.org/10.1098/rsif.2019.0735>
- Escrevente, C., Falcão, A. S., Hall, M. J., Lopes-da-Silva, M., Antas, P., Mesquita, M. M., Ferreira, I. S., Cardoso, M. H., Oliveira, D., Fradinho, A. C., Ciossek, T., Nicklin, P., Futter, C. E., Tenreiro, S., & Seabra, M. C. (2021). Formation of Lipofuscin-Like Autofluorescent Granules in the Retinal Pigment Epithelium Requires Lysosome Dysfunction. *Investigative Ophthalmology & Visual Science*, 62(9), 39. <https://doi.org/10.1167/iovs.62.9.39>
- Fader Kaiser, C. M., Romano, P. S., Vanrell, M. C., Pocognoni, C. A., Jacob, J., Caruso, B., & Delgui, L. R. (2022). Biogenesis and Breakdown of Lipid Droplets in Pathological Conditions. *Frontiers in Cell and Developmental Biology*, 9, 826248. <https://doi.org/10.3389/fcell.2021.826248>
- Farnoodian, M., Bose, D., Barone, F., Nelson, L. M., Boyle, M., Jun, B., Do, K., Gordon, W., Guerin, M.-A. K., Perera, R., Ji, J. X., Cogliati, T., Sharma, R., Brooks, B. P., Bazan, N. G., & Bharti, K. (2023). Retina and RPE lipid profile changes linked with ABCA4 associated Stargardt's maculopathy. *Pharmacology & Therapeutics*, 249, 108482. <https://doi.org/10.1016/j.pharmthera.2023.108482>

- Farnoodian, M., Bose, D., Khristov, V., Susaimanickam, P. J., Maddileti, S., Mariappan, I., Abu-Asab, M., Campos, M., Villasmil, R., Wan, Q., Maminishkis, A., McGaughey, D., Barone, F., Gundry, R. L., Riordon, D. R., Boheler, K. R., Sharma, R., & Bharti, K. (2022). Cell-autonomous lipid-handling defects in Stargardt iPSC-derived retinal pigment epithelium cells. *Stem Cell Reports*, *17*(11), 2438–2450.
<https://doi.org/10.1016/j.stemcr.2022.10.001>
- Feng, P., Skowrya, M. L., & Rapoport, T. A. (2022). Structure and function of the peroxisomal ubiquitin ligase complex. *Biochemical Society Transactions*, *50*(6), 1921–1930. <https://doi.org/10.1042/BST20221393>
- Feng, P., Wu, X., Erramilli, S. K., Paulo, J. A., Knejski, P., Gygi, S. P., Kossiakoff, A. A., & Rapoport, T. A. (2022). A peroxisomal ubiquitin ligase complex forms a retrotranslocation channel. *Nature*, *607*(7918), 374–380.
<https://doi.org/10.1038/s41586-022-04903-x>
- Fletcher, E. L., Greferath, U., Guennel, P., Huynh, M., Findlay, Q. D., Jobling, A. I., Phipps, J. A., Brandli, A. A., Wang, Y. M., Mills, S. A., Kakavand, K., Delongh, R. U., & Vessey, K. A. (2020). Animal Models of Diseases of the Retinal Pigment Epithelium. In A. K. Klettner & S. Dithmar (Eds.), *Retinal Pigment Epithelium in Health and Disease* (pp. 325–347). Springer International Publishing. https://doi.org/10.1007/978-3-030-28384-1_19
- Fliesler, A. J., & Anderson, R. E. (1983). Chemistry and metabolism of lipids in the vertebrate retina. *Progress in Lipid Research*, *22*(2), 79–131.
[https://doi.org/10.1016/0163-7827\(83\)90004-8](https://doi.org/10.1016/0163-7827(83)90004-8)
- Fu, Z., Kern, T. S., Hellström, A., & Smith, L. E. H. (2021). Fatty acid oxidation and photoreceptor metabolic needs. *Journal of Lipid Research*, *62*, 100035.
<https://doi.org/10.1194/jlr.TR120000618>
- Fujiki, Y., Abe, Y., Imoto, Y., Tanaka, A. J., Okumoto, K., Honsho, M., Tamura, S., Miyata, N., Yamashita, T., Chung, W. K., & Kuroiwa, T. (2020). Recent insights into peroxisome biogenesis and associated diseases. *Journal of Cell Science*, *133*(9).
<https://doi.org/10.1242/jcs.236943>

- Gao, Y., Skowrya, M. L., Feng, P., & Rapoport, T. A. (2022). Protein import into peroxisomes occurs through a nuclear pore-like phase. *Science*, 378(6625), eadf3971. <https://doi.org/10.1126/science.adf3971>
- Gargiulo, A., Testa, F., Rossi, S., Di Iorio, V., Fecarotta, S., De Berardinis, T., Iovine, A., Magli, A., Signorini, S., Fazzi, E., Galantuomo, M. S., Fossarello, M., Montefusco, S., Ciccodicola, A., Neri, A., Macaluso, C., Simonelli, F., & Surace, E. M. (2011). Molecular and Clinical Characterization of Albinism in a Large Cohort of Italian Patients. *Investigative Ophthalmology & Visual Science*, 52(3), 1281. <https://doi.org/10.1167/iovs.10-6091>
- Goldberg, A. F. X., Moritz, O. L., & Williams, D. S. (2016). Molecular basis for photoreceptor outer segment architecture. *Progress in Retinal and Eye Research*, 55, 52–81. <https://doi.org/10.1016/j.preteyeres.2016.05.003>
- Han, S.-I., Nakakuki, M., Nakagawa, Y., Wang, Y., Araki, M., Yamamoto, Y., Tokiwa, H., Takeda, H., Mizunoe, Y., Motomura, K., Ohno, H., Kainoh, K., Murayama, Y., Aita, Y., Takeuchi, Y., Osaki, Y., Miyamoto, T., Sekiya, M., Matsuzaka, T., ... Shimano, H. (2023). Rhomboid protease RHBDL4/RHBDD1 cleaves SREBP-1c at endoplasmic reticulum monitoring and regulating fatty acids. *PNAS Nexus*, 2(11), pgad351. <https://doi.org/10.1093/pnasnexus/pgad351>
- Hartzell, H. C., Qu, Z., Yu, K., Xiao, Q., & Chien, L.-T. (2008). Molecular Physiology of Bestrophins: Multifunctional Membrane Proteins Linked to Best Disease and Other Retinopathies. *Physiological Reviews*, 88(2), 639–672. <https://doi.org/10.1152/physrev.00022.2007>
- Hazim, R. A., Volland, S., Yen, A., Burgess, B. L., & Williams, D. S. (2019). Rapid differentiation of the human RPE cell line, ARPE-19, induced by nicotinamide. *Experimental Eye Research*, 179, 18–24. <https://doi.org/10.1016/j.exer.2018.10.009>
- Heid, H. W., Moll, R., Schwetlick, I., Rackwitz, H.-R., & Keenan, T. W. (1998). Adipophilin is a specific marker of lipid accumulation in diverse cell types and diseases. *Cell and Tissue Research*, 294(2), 309–321. <https://doi.org/10.1007/s004410051181>

- Henne, W. M., Reese, M. L., & Goodman, J. M. (2018). The assembly of lipid droplets and their roles in challenged cells. *The EMBO Journal*, *37*(12), e98947. <https://doi.org/10.15252/emj.201898947>
- Herzog, K., Pras-Raves, M. L., Ferdinandusse, S., Vervaart, M. A. T., Luyf, A. C. M., Van Kampen, A. H. C., Wanders, R. J. A., Waterham, H. R., & Vaz, F. M. (2018). Plasma lipidomics as a diagnostic tool for peroxisomal disorders. *Journal of Inherited Metabolic Disease*, *41*(3), 489–498. <https://doi.org/10.1007/s10545-017-0114-7>
- Hua, R., Cheng, D., Coyaud, É., Freeman, S., Di Pietro, E., Wang, Y., Vissa, A., Yip, C. M., Fairn, G. D., Braverman, N., Brumell, J. H., Trimble, W. S., Raught, B., & Kim, P. K. (2017). VAPs and ACBD5 tether peroxisomes to the ER for peroxisome maintenance and lipid homeostasis. *Journal of Cell Biology*, *216*(2), 367–377. <https://doi.org/10.1083/jcb.201608128>
- Jones, J. M., Morrell, J. C., & Gould, S. J. (2004). PEX19 is a predominantly cytosolic chaperone and import receptor for class 1 peroxisomal membrane proteins. *The Journal of Cell Biology*, *164*(1), 57–67. <https://doi.org/10.1083/jcb.200304111>
- Judy, R. M., Sheedy, C. J., & Gardner, B. M. (2022). Insights into the Structure and Function of the Pex1/Pex6 AAA-ATPase in Peroxisome Homeostasis. *Cells*, *11*(13), 2067. <https://doi.org/10.3390/cells11132067>
- Kanow, M. A., Giarmarco, M. M., Jankowski, C. S., Tsantilas, K., Engel, A. L., Du, J., Linton, J. D., Farnsworth, C. C., Sloat, S. R., Rountree, A., Sweet, I. R., Lindsay, K. J., Parker, E. D., Brockerhoff, S. E., Sadilek, M., Chao, J. R., & Hurley, J. B. (2017). Biochemical adaptations of the retina and retinal pigment epithelium support a metabolic ecosystem in the vertebrate eye. *eLife*, *6*, e28899. <https://doi.org/10.7554/eLife.28899>
- Kennedy, C. J., Rakoczy, P. E., & Constable, I. J. (1995). Lipofuscin of the retinal pigment epithelium: A review. *Eye*, *9*(6), 763–771. <https://doi.org/10.1038/eye.1995.192>
- Kevany, B. M., & Palczewski, K. (2010). Phagocytosis of Retinal Rod and Cone Photoreceptors. *Physiology*, *25*(1). <https://doi.org/10.1152/physiol.00038.2009>
- Klouwer, F. C. C., Berendse, K., Ferdinandusse, S., Wanders, R. J. A., Engelen, M., & Poll-The, B. T. (2015). Zellweger spectrum disorders: Clinical overview and

- management approach. *Orphanet Journal of Rare Diseases*, 10(1), 151.
<https://doi.org/10.1186/s13023-015-0368-9>
- Kocherlakota, S., Das, Y., Swinkels, D., Vanmunster, M., Callens, M., Vinckier, S., Vaz, F. M., Sinha, D., Van Veldhoven, P. P., Fransen, M., & Baes, M. (2023). The murine retinal pigment epithelium requires peroxisomal β -oxidation to maintain lysosomal function and prevent dedifferentiation. *Proceedings of the National Academy of Sciences*, 120(43), e2301733120. <https://doi.org/10.1073/pnas.2301733120>
- Kong, J., Ji, Y., Jeon, Y. G., Han, J. S., Han, K. H., Lee, J. H., Lee, G., Jang, H., Choe, S. S., Baes, M., & Kim, J. B. (2020). Spatiotemporal contact between peroxisomes and lipid droplets regulates fasting-induced lipolysis via PEX5. *Nature Communications*, 11(1), 578. <https://doi.org/10.1038/s41467-019-14176-0>
- Korotkova, D., Borisjuk, A., Guihur, A., Bardyn, M., Kuttler, F., Reymond, L., Schuhmacher, M., & Amen, T. (2024). Fluorescent fatty acid conjugates for live cell imaging of peroxisomes. *Nature Communications*, 15(1), 4314.
<https://doi.org/10.1038/s41467-024-48679-2>
- Kurochkin, I. V., Mizuno, Y., Konagaya, A., Sakaki, Y., Schönbach, C., & Okazaki, Y. (2007). Novel peroxisomal protease Tysnd1 processes PTS1- and PTS2-containing enzymes involved in β -oxidation of fatty acids. *The EMBO Journal*, 26(3), 835–845. <https://doi.org/10.1038/sj.emboj.7601525>
- Kwon, W., & Freeman, S. A. (2020). Phagocytosis by the Retinal Pigment Epithelium: Recognition, Resolution, Recycling. *Frontiers in Immunology*, 11.
<https://doi.org/10.3389/fimmu.2020.604205>
- Lahola-Chomiak, A. A., Footz, T., Nguyen-Phuoc, K., Neil, G. J., Fan, B., Allen, K. F., Greenfield, D. S., Parrish, R. K., Linkroum, K., Pasquale, L. R., Leonhardt, R. M., Ritch, R., Javadiyan, S., Craig, J. E., Allison, W. T., Lehmann, O. J., Walter, M. A., & Wiggs, J. L. (2019). Non-Synonymous variants in premelanosome protein (PMEL) cause ocular pigment dispersion and pigmentary glaucoma. *Human Molecular Genetics*, 28(8), 1298–1311. <https://doi.org/10.1093/hmg/ddy429>

- Lakkaraju, A., Umapathy, A., Tan, L. X., Daniele, L., Philp, N. J., Boesze-Battaglia, K., & Williams, D. S. (2020). The cell biology of the retinal pigment epithelium. *Progress in Retinal and Eye Research*, 78. <https://doi.org/10.1016/j.preteyeres.2020.100846>
- Landowski, M., Bhute, V. J., Grindel, S., Haugstad, Z., Gyening, Y. K., Tytanic, M., Brush, R. S., Moyer, L. J., Nelson, D. W., Davis, C. R., Yen, C.-L. E., Ikeda, S., Agbaga, M.-P., & Ikeda, A. (2023). Transmembrane protein 135 regulates lipid homeostasis through its role in peroxisomal DHA metabolism. *Communications Biology*, 6(1), 8. <https://doi.org/10.1038/s42003-022-04404-7>
- Landowski, M., Grindel, S., Shahi, P. K., Johnson, A., Western, D., Race, A., Shi, F., Benson, J., Gao, M., Santoirre, E., Lee, W.-H., Ikeda, S., Pattnaik, B. R., & Ikeda, A. (2020). Modulation of *Tmem135* Leads to Retinal Pigmented Epithelium Pathologies in Mice. *Investigative Ophthalmology & Visual Science*, 61(12), 16. <https://doi.org/10.1167/iovs.61.12.16>
- Law, K. B., Bronte-Tinkew, D., Di Pietro, E., Snowden, A., Jones, R. O., Moser, A., Brumell, J. H., Braverman, N., & Kim, P. K. (2017). The peroxisomal AAA ATPase complex prevents pexophagy and development of peroxisome biogenesis disorders. *Autophagy*, 13(5), 868–884. <https://doi.org/10.1080/15548627.2017.1291470>
- Lewandowski, D., Sander, C. L., Tworak, A., Gao, F., Xu, Q., & Skowronska-Krawczyk, D. (2022). Dynamic lipid turnover in photoreceptors and retinal pigment epithelium throughout life. *Progress in Retinal and Eye Research*, 89, 101037. <https://doi.org/10.1016/j.preteyeres.2021.101037>
- Li, X., Krawetz, R., Liu, S., Meng, G., & Rancourt, D. E. (2008). ROCK inhibitor improves survival of cryopreserved serum/feeder-free single human embryonic stem cells. *Human Reproduction*, 24(3), 580–589. <https://doi.org/10.1093/humrep/den404>
- Listenberger, L. L., Studer, A. M., Brown, D. A., & Wolins, N. E. (2016). Fluorescent Detection of Lipid Droplets and Associated Proteins. *Current Protocols in Cell Biology*, 71(1). <https://doi.org/10.1002/cpcb.7>
- Lu, Q., Zong, W., Zhang, M., Chen, Z., & Yang, Z. (2022). The Overlooked Transformation Mechanisms of VLCFAs: Peroxisomal β -Oxidation. *Agriculture*, 12(7), 947. <https://doi.org/10.3390/agriculture12070947>

- Lukovic, D., Artero Castro, A., Delgado, A. B. G., Bernal, M. D. L. A. M., Luna Pelaez, N., Díez Lloret, A., Perez Espejo, R., Kamenarova, K., Fernández Sánchez, L., Cuenca, N., Cortón, M., Avila Fernandez, A., Sorkio, A., Skottman, H., Ayuso, C., Erceg, S., & Bhattacharya, S. S. (2015). Human iPSC derived disease model of MERTK-associated retinitis pigmentosa. *Scientific Reports*, 5(1), 12910. <https://doi.org/10.1038/srep12910>
- Luo, Y., Zhuo, Y., Fukuhara, M., & Rizzolo, L. J. (2006). Effects of Culture Conditions on Heterogeneity and the Apical Junctional Complex of the ARPE-19 Cell Line. *Investigative Ophthalmology & Visual Science*, 47(8), 3644. <https://doi.org/10.1167/iovs.06-0166>
- Marcheselli, V. L., Mukherjee, P. K., Arita, M., Hong, S., Antony, R., Sheets, K., Winkler, J. W., Petasis, N. A., Serhan, C. N., & Bazan, N. G. (2010). Neuroprotectin D1/protectin D1 stereoselective and specific binding with human retinal pigment epithelial cells and neutrophils. *Prostaglandins, Leukotrienes and Essential Fatty Acids*, 82(1), 27–34. <https://doi.org/10.1016/j.plefa.2009.10.010>
- Marmorstein, A. D., Marmorstein, L. Y., Rayborn, M., Wang, X., Hollyfield, J. G., & Petrukhin, K. (2000). Bestrophin, the product of the Best vitelliform macular dystrophy gene (*VMD2*), localizes to the basolateral plasma membrane of the retinal pigment epithelium. *Proceedings of the National Academy of Sciences*, 97(23), 12758–12763. <https://doi.org/10.1073/pnas.220402097>
- Mazzoni, F., Mao, Y., & Finnemann, S. C. (2019). Advanced Analysis of Photoreceptor Outer Segment Phagocytosis by RPE Cells in Culture. In B. H. F. Weber & T. Langmann (Eds.), *Retinal Degeneration* (Vol. 1834, pp. 95–108). Springer New York. https://doi.org/10.1007/978-1-4939-8669-9_7
- McIntosh, A. L., Senthivayagam, S., Moon, K. C., Gupta, S., Lwande, J. S., Murphy, C. C., Storey, S. M., & Atshaves, B. P. (2012). Direct interaction of Plin2 with lipids on the surface of lipid droplets: A live cell FRET analysis. *American Journal of Physiology-Cell Physiology*, 303(7), C728–C742. <https://doi.org/10.1152/ajpcell.00448.2011>

- Mizuno, Y., Ninomiya, Y., Nakachi, Y., Iseki, M., Iwasa, H., Akita, M., Tsukui, T., Shimozawa, N., Ito, C., Toshimori, K., Nishimukai, M., Hara, H., Maeba, R., Okazaki, T., Alodaib, A. N. A., Amoudi, M. A., Jacob, M., Alkuraya, F. S., Horai, Y., ... Okazaki, Y. (2013). Tysnd1 Deficiency in Mice Interferes with the Peroxisomal Localization of PTS2 Enzymes, Causing Lipid Metabolic Abnormalities and Male Infertility. *PLoS Genetics*, 9(2), e1003286. <https://doi.org/10.1371/journal.pgen.1003286>
- Muntau, A. C., Mayerhofer, P. U., Paton, B. C., Kammerer, S., & Roscher, A. A. (2000). Defective Peroxisome Membrane Synthesis Due To Mutations in Human PEX3 Causes Zellweger Syndrome, Complementation Group G. *The American Journal of Human Genetics*, 67(4), 967–975. <https://doi.org/10.1086/303071>
- Nandrot, E. F. (2014). Animal Models, in “The Quest to Decipher RPE Phagocytosis.” In J. D. Ash, C. Grimm, J. G. Hollyfield, R. E. Anderson, M. M. LaVail, & C. Bowes Rickman (Eds.), *Retinal Degenerative Diseases* (Vol. 801, pp. 77–83). Springer New York. https://doi.org/10.1007/978-1-4614-3209-8_10
- Nguyen, H., Li, Y., & Tsang, S. (2015). Patient-Specific iPSC-Derived RPE for Modeling of Retinal Diseases. *Journal of Clinical Medicine*, 4(4), 567–578. <https://doi.org/10.3390/jcm4040567>
- Nolan, N., Jenny, L., Wang, N.-K., & Tsang, S. (2021). Retinal pigment epithelium lipid metabolic demands and therapeutic restoration. *Taiwan Journal of Ophthalmology*, 11(3), 216. https://doi.org/10.4103/tjo.tjo_31_21
- Ohgushi, M., Matsumura, M., Eiraku, M., Murakami, K., Aramaki, T., Nishiyama, A., Muguruma, K., Nakano, T., Suga, H., Ueno, M., Ishizaki, T., Suemori, H., Narumiya, S., Niwa, H., & Sasai, Y. (2010). Molecular Pathway and Cell State Responsible for Dissociation-Induced Apoptosis in Human Pluripotent Stem Cells. *Cell Stem Cell*, 7(2), 225–239. <https://doi.org/10.1016/j.stem.2010.06.018>
- Ortolan, D., Volkov, A., Maminishkis, A., Sharma, R., & Bharti, K. (2022). Efficient and Consistent Generation of Retinal Pigment Epithelium/Choroid Flatmounts from Human Eyes for Histological Analysis. *Journal of Visualized Experiments*, 188, 64761. <https://doi.org/10.3791/64761>

- Ott, J., Sehr, J., Schmidt, N., Schliebs, W., & Erdmann, R. (2023). Comparison of human PEX knockout cell lines suggests a dual role of PEX1 in peroxisome biogenesis. *Biological Chemistry*, 404(2–3), 209–219. <https://doi.org/10.1515/hsz-2022-0223>
- Parinot, C., Rieu, Q., Chatagnon, J., Finnemann, S. C., & Nandrot, E. F. (2014). Large-Scale Purification of Porcine or Bovine Photoreceptor Outer Segments for Phagocytosis Assays on Retinal Pigment Epithelial Cells. *Journal of Visualized Experiments*, 94, 52100. <https://doi.org/10.3791/52100>
- Pearsall, E. A., Cheng, R., Zhou, K., Takahashi, Y., Matlock, H. G., Vadvalkar, S. S., Shin, Y., Fredrick, T. W., Gantner, M. L., Meng, S., Fu, Z., Gong, Y., Kinter, M., Humphries, K. M., Szweda, L. I., Smith, L. E. H., & Ma, J. (2017). PPAR α is essential for retinal lipid metabolism and neuronal survival. *BMC Biology*, 15(1), 113. <https://doi.org/10.1186/s12915-017-0451-x>
- Perrotta, I. (2017). Interaction between lipid droplets and endoplasmic reticulum in human atherosclerotic plaques. *Ultrastructural Pathology*, 41(1), 1–9. <https://doi.org/10.1080/01913123.2016.1269861>
- Petriv, O. I., Tang, L., Titorenko, V. I., & Rachubinski, R. A. (2004). A New Definition for the Consensus Sequence of the Peroxisome Targeting Signal Type 2. *Journal of Molecular Biology*, 341(1), 119–134. <https://doi.org/10.1016/j.jmb.2004.05.064>
- Pfeffer, B. A., & Fliesler, S. J. (2022). Reassessing the suitability of ARPE-19 cells as a valid model of native RPE biology. *Experimental Eye Research*, 219, 109046. <https://doi.org/10.1016/j.exer.2022.109046>
- Qiu, B., & Simon, M. (2016). BODIPY 493/503 Staining of Neutral Lipid Droplets for Microscopy and Quantification by Flow Cytometry. *BIO-PROTOCOL*, 6(17). <https://doi.org/10.21769/BioProtoc.1912>
- Ramsden, C. M., Nommiste, B., R. Lane, A., Carr, A.-J. F., Powner, M. B., J. K. Smart, M., Chen, L. L., Muthiah, M. N., Webster, A. R., Moore, A. T., Cheetham, M. E., Da Cruz, L., & Coffey, P. J. (2017). Rescue of the MERTK phagocytic defect in a human iPSC disease model using translational read-through inducing drugs. *Scientific Reports*, 7(1), 51. <https://doi.org/10.1038/s41598-017-00142-7>

- Ranea-Robles, P., Chen, H., Stauffer, B., Yu, C., Bhattacharya, D., Friedman, S. L., Puchowicz, M., & Houten, S. M. (2021). The peroxisomal transporter ABCD3 plays a major role in hepatic dicarboxylic fatty acid metabolism and lipid homeostasis. *Journal of Inherited Metabolic Disease*, *44*(6), 1419–1433. <https://doi.org/10.1002/jimd.12440>
- Raviv, S., Bharti, K., Rencus-Lazar, S., Cohen-Tayar, Y., Schyr, R., Evantal, N., Meshorer, E., Zilberberg, A., Idelson, M., Reubinoff, B., Grebe, R., Rosin-Arbesfeld, R., Lauderdale, J., Lutty, G., Arnheiter, H., & Ashery-Padan, R. (2014). PAX6 Regulates Melanogenesis in the Retinal Pigmented Epithelium through Feed-Forward Regulatory Interactions with MITF. *PLoS Genetics*, *10*(5), e1004360. <https://doi.org/10.1371/journal.pgen.1004360>
- Regent, F., Morizur, L., Lesueur, L., Habeler, W., Plancheron, A., Ben M'Barek, K., & Monville, C. (2019). Automation of human pluripotent stem cell differentiation toward retinal pigment epithelial cells for large-scale productions. *Scientific Reports*, *9*(1), 10646. <https://doi.org/10.1038/s41598-019-47123-6>
- Reyes-Reveles, J., Dhingra, A., Alexander, D., Bragin, A., Philp, N. J., & Boesze-Battaglia, K. (2017). Phagocytosis-dependent ketogenesis in retinal pigment epithelium. *Journal of Biological Chemistry*, *292*(19). <https://doi.org/10.1074/jbc.M116.770784>
- Rinaldi, M. A., Fleming, W. A., Gonzalez, K. L., Park, J., Ventura, M. J., Patel, A. B., & Bartel, B. (2017). The PEX1 ATPase Stabilizes PEX6 and Plays Essential Roles in Peroxisome Biology. *Plant Physiology*, *174*(4), 2231–2247. <https://doi.org/10.1104/pp.17.00548>
- Rotstein, N. P., Politi, L. E., German, O. L., & Girotti, R. (2003). Protective Effect of Docosahexaenoic Acid on Oxidative Stress-Induced Apoptosis of Retina Photoreceptors. *Investigative Ophthalmology & Visual Science*, *44*(5), 2252. <https://doi.org/10.1167/iovs.02-0901>
- Sarangarajan, R., & Boissy, R. E. (2001). Tyrp1 and Oculocutaneous Albinism Type 3. *Pigment Cell Research*, *14*(6), 437–444. <https://doi.org/10.1034/j.1600-0749.2001.140603.x>

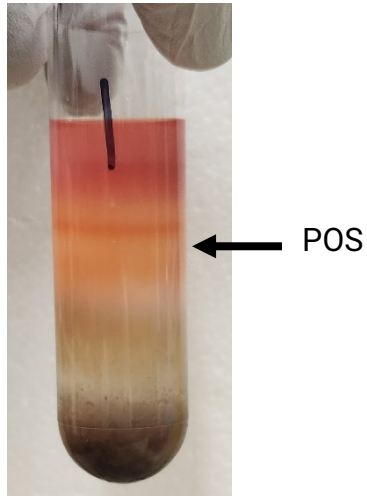
- Sharma, R., Bose, D., Montford, J., Ortolan, D., & Bharti, K. (2022). Triphasic developmentally guided protocol to generate retinal pigment epithelium from induced pluripotent stem cells. *STAR Protocols*, 3(3).
<https://doi.org/10.1016/j.xpro.2022.101582>
- Sharma, R., Khristov, V., Rising, A., Jha, B. S., Dejene, R., Hotaling, N., Li, Y., Stoddard, J., Stankewicz, C., Wan, Q., Zhang, C., Campos, M. M., Miyagishima, K. J., McGaughey, D., Villasmil, R., Mattapallil, M., Stanzel, B., Qian, H., Wong, W., ... Bharti, K. (2019). Clinical-grade stem cell–derived retinal pigment epithelium patch rescues retinal degeneration in rodents and pigs. *Science Translational Medicine*, 11(475), eaat5580. <https://doi.org/10.1126/scitranslmed.aat5580>
- Sinha, T., Naash, M. I., & Al-Ubaidi, M. R. (2020). The Symbiotic Relationship between the Neural Retina and Retinal Pigment Epithelium Is Supported by Utilizing Differential Metabolic Pathways. *iScience*, 23(4), 101004.
<https://doi.org/10.1016/j.isci.2020.101004>
- Stone, W. L., Farnsworth, C. C., & Dratz, E. A. (1979). A reinvestigation of the fatty acid content of bovine, rat and frog retinal rod outer segments. *Experimental Eye Research*, 28(4), 387–397. [https://doi.org/10.1016/0014-4835\(79\)90114-3](https://doi.org/10.1016/0014-4835(79)90114-3)
- Strauss, O. (2005). The Retinal Pigment Epithelium in Visual Function. *Physiological Reviews*, 85(3), 845–881. <https://doi.org/10.1152/physrev.00021.2004>
- Subramani, S. (1998). Components Involved in Peroxisome Import, Biogenesis, Proliferation, Turnover, and Movement. *Physiological Reviews*, 78(1), 171–188.
<https://doi.org/10.1152/physrev.1998.78.1.171>
- Swarup, A., Samuels, I. S., Bell, B. A., Han, J. Y. S., Du, J., Massenzio, E., Abel, E. D., Boesze-Battaglia, K., Peachey, N. S., & Philp, N. J. (2019). Modulating GLUT1 expression in retinal pigment epithelium decreases glucose levels in the retina: Impact on photoreceptors and Müller glial cells. *American Journal of Physiology-Cell Physiology*, 316(1), C121–C133. <https://doi.org/10.1152/ajpcell.00410.2018>
- Swinkels, D., & Baes, M. (2023). The essential role of docosahexaenoic acid and its derivatives for retinal integrity. *Pharmacology & Therapeutics*, 247, 108440.
<https://doi.org/10.1016/j.pharmthera.2023.108440>

- Swinkels, D., Kocherlakota, S., Das, Y., Dane, A. D., Wever, E. J. M., Vaz, F. M., Bazan, N. G., Van Veldhoven, P. P., & Baes, M. (2023). DHA Shortage Causes the Early Degeneration of Photoreceptors and RPE in Mice With Peroxisomal β -Oxidation Deficiency. *Investigative Ophthalmology & Visual Science*, 64(14), 10. <https://doi.org/10.1167/iovs.64.14.10>
- Sztalryd, C., & Brasaemle, D. L. (2017). The perilipin family of lipid droplet proteins: Gatekeepers of intracellular lipolysis. *Biochimica et Biophysica Acta (BBA) - Molecular and Cell Biology of Lipids*, 1862(10), 1221–1232. <https://doi.org/10.1016/j.bbalip.2017.07.009>
- Tan, A. P., Gonçalves, F. G., Almeshdar, A., & Soares, B. P. (2018). Clinical and Neuroimaging Spectrum of Peroxisomal Disorders. *Topics in Magnetic Resonance Imaging*, 27(4), 241–257. <https://doi.org/10.1097/RMR.0000000000000172>
- Thelen, A. M., & Zoncu, R. (2017). Emerging Roles for the Lysosome in Lipid Metabolism. *Trends in Cell Biology*, 27(11), 833–850. <https://doi.org/10.1016/j.tcb.2017.07.006>
- Tsukamoto, T., Hata, S., Yokota, S., Miura, S., Fujiki, Y., Hijikata, M., Miyazawa, S., Hashimoto, T., & Osumi, T. (1994). Characterization of the signal peptide at the amino terminus of the rat peroxisomal 3-ketoacyl-CoA thiolase precursor. *Journal of Biological Chemistry*, 269(8), 6001–6010. [https://doi.org/10.1016/S0021-9258\(17\)37561-0](https://doi.org/10.1016/S0021-9258(17)37561-0)
- Umapathy, A., Torten, G., Paniagua, A. E., Chung, J., Tomlinson, M., Lim, C., & Williams, D. S. (2023). Spatiotemporal Live-Cell Analysis of Photoreceptor Outer Segment Membrane Ingestion by the Retinal Pigment Epithelium Reveals Actin-Regulated Scission. *The Journal of Neuroscience*, 43(15), 2653–2664. <https://doi.org/10.1523/JNEUROSCI.1726-22.2023>
- Van Roermund, C. W. T., IJlst, L., Wagemans, T., Wanders, R. J. A., & Waterham, H. R. (2014). A role for the human peroxisomal half-transporter ABCD3 in the oxidation of dicarboxylic acids. *Biochimica et Biophysica Acta (BBA) - Molecular and Cell Biology of Lipids*, 1841(4), 563–568. <https://doi.org/10.1016/j.bbalip.2013.12.001>

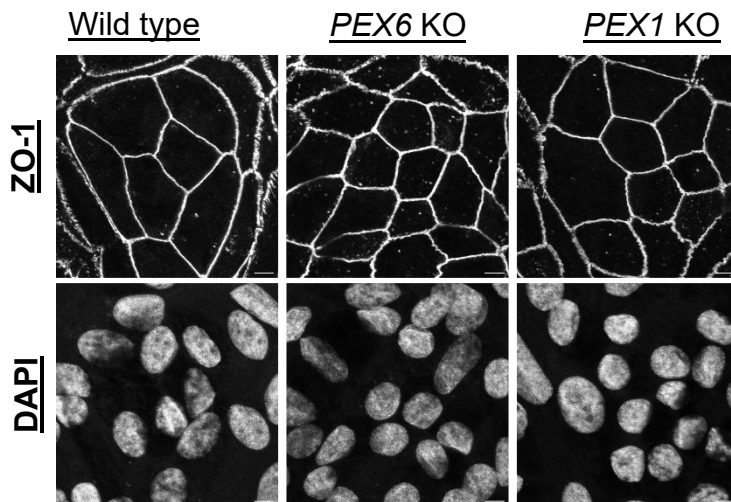
- Ventura, M. J., Wheaton, D., Xu, M., Birch, D., Bowne, S. J., Sullivan, L. S., Daiger, S. P., Whitney, A. E., Jones, R. O., Moser, A. B., Chen, R., & Wangler, M. F. (2016). Diagnosis of a mild peroxisomal phenotype with next-generation sequencing. *Molecular Genetics and Metabolism Reports*, *9*, 75–78. <https://doi.org/10.1016/j.ymgmr.2016.10.006>
- Violante, S., Achetib, N., Roermund, C. W. T., Hagen, J., Dodatko, T., Vaz, F. M., Waterham, H. R., Chen, H., Baes, M., Yu, C., Argmann, C. A., & Houten, S. M. (2019). Peroxisomes can oxidize medium- and long-chain fatty acids through a pathway involving ABCD3 and HSD17B4. *The FASEB Journal*, *33*(3), 4355–4364. <https://doi.org/10.1096/fj.201801498R>
- Walker, A., Su, H., Conti, M. A., Harb, N., Adelstein, R. S., & Sato, N. (2010). Non-muscle myosin II regulates survival threshold of pluripotent stem cells. *Nature Communications*, *1*(1), 71. <https://doi.org/10.1038/ncomms1074>
- Wanders, R. J. A., Baes, M., Ribeiro, D., Ferdinandusse, S., & Waterham, H. R. (2023). The physiological functions of human peroxisomes. *Physiological Reviews*, *103*(1), 957–1024. <https://doi.org/10.1152/physrev.00051.2021>
- Wang, W., & Subramani, S. (2017). Role of PEX5 ubiquitination in maintaining peroxisome dynamics and homeostasis. *Cell Cycle*, *16*(21), 2037–2045. <https://doi.org/10.1080/15384101.2017.1376149>
- Waterham, H. R., Ferdinandusse, S., & Wanders, R. J. A. (2016). Human disorders of peroxisome metabolism and biogenesis. *Biochimica et Biophysica Acta (BBA) - Molecular Cell Research*, *1863*(5), 922–933. <https://doi.org/10.1016/j.bbamcr.2015.11.015>
- Wu, W., Zeng, Y., Li, Z., Li, Q., Xu, H., & Yin, Z. Q. (2016). Features specific to retinal pigment epithelium cells derived from three-dimensional human embryonic stem cell cultures—A new donor for cell therapy. *Oncotarget*, *7*(16), 22819–22833. <https://doi.org/10.18632/oncotarget.8185>
- Xu, Y., Zhu, X., Hahm, H. S., Wei, W., Hao, E., Hayek, A., & Ding, S. (2010). Revealing a core signaling regulatory mechanism for pluripotent stem cell survival and self-

- renewal by small molecules. *Proceedings of the National Academy of Sciences*, 107(18), 8129–8134. <https://doi.org/10.1073/pnas.1002024107>
- Yako, T., Otsu, W., Nakamura, S., Shimazawa, M., & Hara, H. (2022). Lipid Droplet Accumulation Promotes RPE Dysfunction. *International Journal of Molecular Sciences*, 23(3), 1790. <https://doi.org/10.3390/ijms23031790>
- Young, R. W. (1967). THE RENEWAL OF PHOTORECEPTOR CELL OUTER SEGMENTS. *The Journal of Cell Biology*, 33(1), 61–72. <https://doi.org/10.1083/jcb.33.1.61>
- Young, R. W., & Bok, D. (1969). PARTICIPATION OF THE RETINAL PIGMENT EPITHELIUM IN THE ROD OUTER SEGMENT RENEWAL PROCESS. *The Journal of Cell Biology*, 42(2), 392–403. <https://doi.org/10.1083/jcb.42.2.392>
- Zadoorian, A., Du, X., & Yang, H. (2023). Lipid droplet biogenesis and functions in health and disease. *Nature Reviews Endocrinology*, 19(8), 443–459. <https://doi.org/10.1038/s41574-023-00845-0>
- Zhang, T., Huang, X., Liu, S., Bai, X., Zhu, X., Clegg, D. O., Jiang, M., & Sun, X. (2022). Determining the optimal stage for cryopreservation of human embryonic stem cell-derived retinal pigment epithelial cells. *Stem Cell Research & Therapy*, 13(1), 454. <https://doi.org/10.1186/s13287-022-03141-2>
- Zimmermann, R., Strauss, J. G., Haemmerle, G., Schoiswohl, G., Birner-Gruenberger, R., Riederer, M., Lass, A., Neuberger, G., Eisenhaber, F., Hermetter, A., & Zechner, R. (2004). Fat Mobilization in Adipose Tissue Is Promoted by Adipose Triglyceride Lipase. *Science*, 306(5700), 1383–1386. <https://doi.org/10.1126/science.1100747>

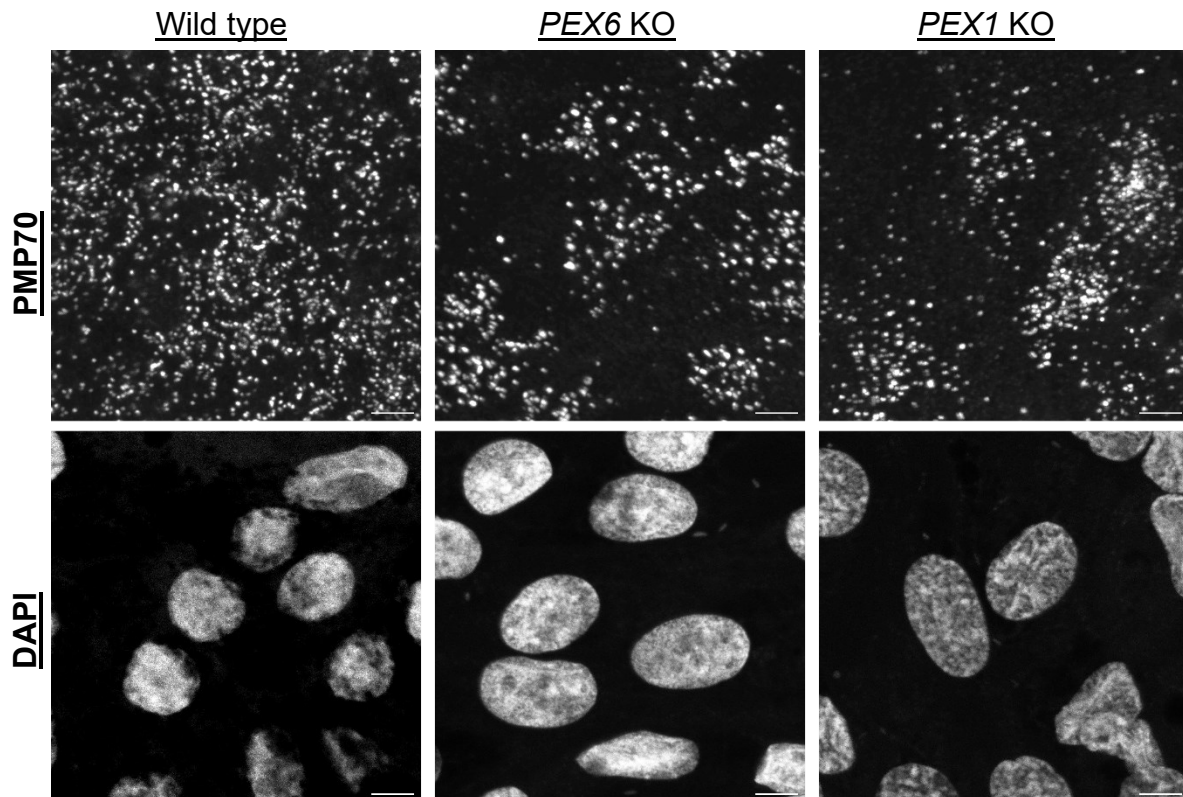
Appendix



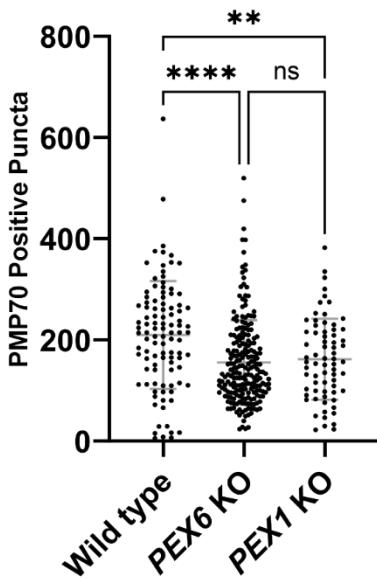
Supplementary Figure 1.
Visualizing photoreceptor outer segments isolated from bovine retinas. The tube is imaged immediately following the centrifugation of the homogenized retina in a sucrose gradient. The arrow highlights the orange photoreceptor outer segment band that was extracted.



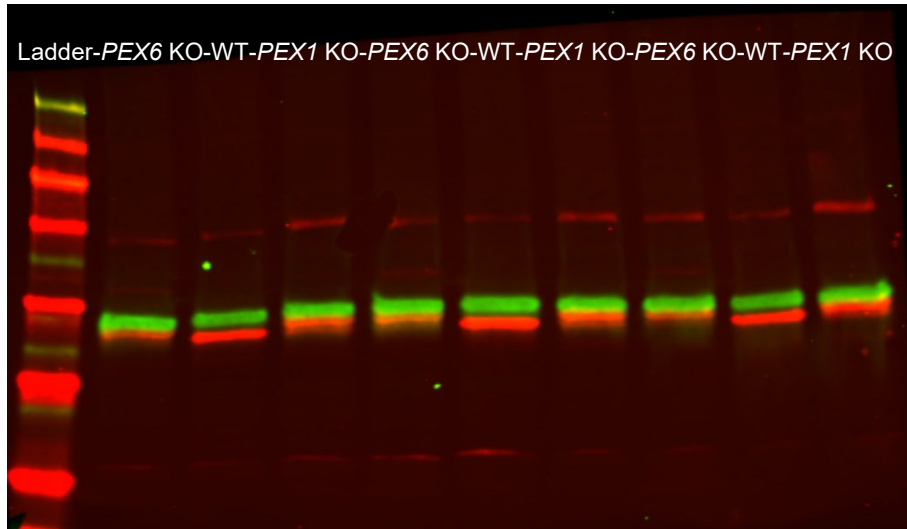
Supplementary Figure 2.
Immunofluorescence detection of ZO-1 in iRPE. Maximum intensity projections of z-stacks were captured using a Leica SP5 confocal microscope. The scale bar is 5 μ m.



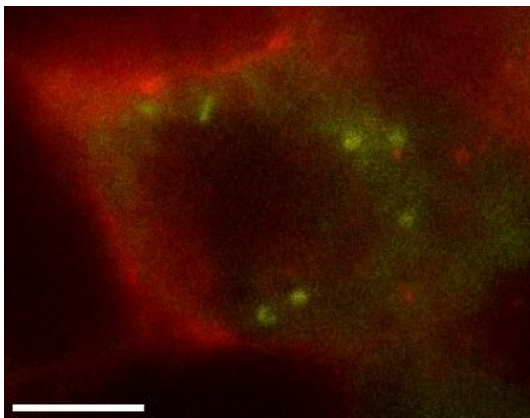
Supplementary Figure 3. Immunofluorescence detection of PMP70 in iRPE. Maximum intensity projections of z-stacks were captured using a Leica SP5 confocal microscope. The scale bar is 5µm.



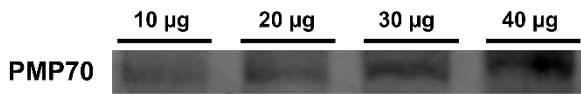
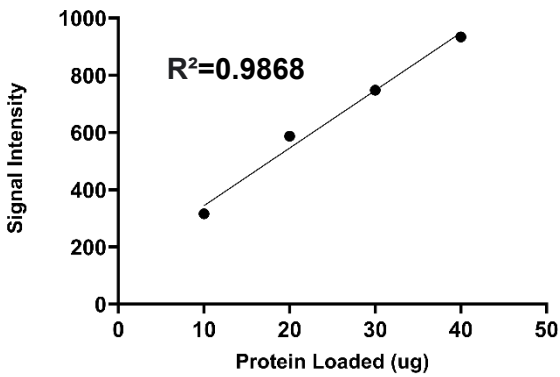
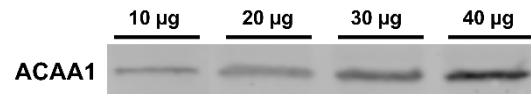
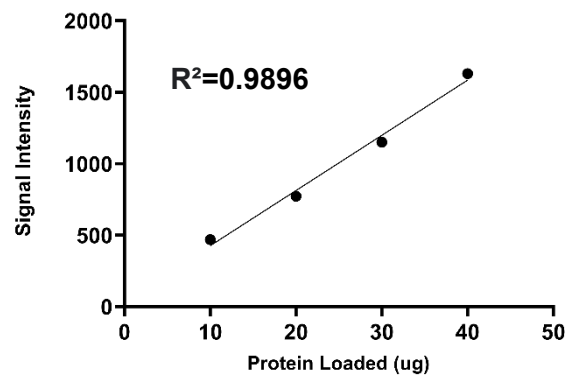
Supplementary Figure 4. Quantification of PMP70-positive puncta in iRPE. If cells were independently considered, a one-way ANOVA is significant $P < 0.0001$. Tukey's comparisons are indicated by ** $P = 0.0018$ and **** $P < 0.0001$ (n=385 cells)



Supplementary Figure 5. Evaluating ACAA1 processing by western blot to assess the integrity of peroxisomal matrix protein import. PTS2-ACAA1 and ACAA1 were probed in iRPE lysates and the images were acquired using a Li-Cor Odyssey CLx. ACAA1 is in red and γ -tubulin is in green and serves as a consistent size marker. The upper and lower red bands are nonspecific antibody signal. The smaller ACAA1 (cleaved) band is detected exclusively in wild-type iRPE. The larger PTS2-ACAA1 (uncleaved) band is detected exclusively in the peroxisome exportomer-deficient (*PEX1* and *PEX6* KO) iRPE (n=3 technical replicates).



Supplementary Figure 6. Immunofluorescence detection of PLIN2 and Claudin-19 in wild-type iRPE fed with POS. PLIN2 is in yellow. Claudin-19 is in red. Single plane image captured using a Leica Thunder microscope. The scale bar is 5 μ m.

A**B**

Supplementary Figure 7. Western blot standard curves for PMP70 and ACAA1. A) anti-PMP70 standard curve and corresponding western blot. B) anti-ACAA1 standard curve and corresponding western blot. Simple linear regression R-squared values are indicated on the graphs.